



AD-A208402

DTIC
SELECTED
JUN 01 1989

REPORT DOCUMENTATION PAGE				
1a. REPORT SECURITY CLASSIFICATION Unclassified		1b. RESTRICTIVE MARKINGS		
2a. SECURITY CLASSIFICATION AUTHORITY		3. DISTRIBUTION / AVAILABILITY OF REPORT Approved for public release: distribution unlimited		
2b. DECLASSIFICATION / DOWNGRADING SCHEDULE		4. PERFORMING ORGANIZATION REPORT NUMBER(S) MDC QA026		
4. PERFORMING ORGANIZATION REPORT NUMBER(S)		5. MONITORING ORGANIZATION REPORT NUMBER(S) AFOSR-TR- 89-0650		
6a. NAME OF PERFORMING ORGANIZATION McDonnell Douglas Research Laboratories	6b. OFFICE SYMBOL (if applicable) MDRL	7a. NAME OF MONITORING ORGANIZATION Air Force Office of Scientific Research		
6c. ADDRESS (City, State, and ZIP Code) P. O. Box 516 St. Louis, MO 63166		7b. ADDRESS (City, State, and ZIP Code) Bolling Air Force Base Washington, DC 20332		
8a. NAME OF FUNDING / SPONSORING ORGANIZATION Air Force Office of Scientific Research	8b. OFFICE SYMBOL (if applicable) AFOSR/NA	9. PROCUREMENT INSTRUMENT IDENTIFICATION NUMBER Contract No. F49620-86-C-0063		
8c. ADDRESS (City, State, and ZIP Code) Bolling Air Force Base Washington, DC 20332		10. SOURCE OF FUNDING NUMBERS		
		PROGRAM ELEMENT NO. 61102F	PROJECT NO. 2307	TASK NO. A4
11. TITLE (Include Security Classification) The Structure of Normal-Shock/Turbulent-Boundary-Layer Interactions Modified by Mass Removal				
12. PERSONAL AUTHOR(S) M. Sajben, M. J. Morris, T. J. Bogar, and J. C. Kroutil				
13a. TYPE OF REPORT Final	13b. TIME COVERED FROM 1Jun86 TO 31Dec88	14. DATE OF REPORT (Year, Month, Day) 1989 February 28	15. PAGE COUNT 53	
16. SUPPLEMENTARY NOTATION (cont A over)				
17. COSATI CODES		18. SUBJECT TERMS (Continue on reverse if necessary and identify by block number)		
FIELD	GROUP	SUB-GROUP		
		transonic flow; shock/boundary-layer interactions		
		two dimensional flow; supersonic inlets; (cdc)		
		mass transfer; bleed systems.		
19. ABSTRACT (Continue on reverse if necessary and identify by block number)				
<p>The effect of mass removal on nominally two-dimensional, normal-shock/turbulent-boundary-layer interactions was investigated experimentally. The flowfield had a freestream approach Mach number of 1.49 and a Reynolds number based on boundary layer momentum thickness of 14,600. Distributed mass removal was imposed over a length of approximately 40 initial displacement thicknesses, the entire bleed zone being located immediately upstream of the shock. Detailed velocity field information was obtained for two flows, using a two-component laser Doppler velocimeter system. The two time mean velocity components and the three Reynolds stress components were determined. The measurements were extended over both supersonic and subsonic regions. Surface pressure information was also obtained.</p> <p>The removed mass flow, averaged over the length of the bleed zone, was 2.5% and 8% of the freestream mass flow, for the two cases investigated.</p> <p style="text-align: right;">(Continued)</p>				
20. DISTRIBUTION / AVAILABILITY OF ABSTRACT <input type="checkbox"/> UNCLASSIFIED/UNLIMITED <input checked="" type="checkbox"/> SAME AS RPT <input type="checkbox"/> DTIC USERS		21. ABSTRACT SECURITY CLASSIFICATION UNCLASSIFIED		
22a. NAME OF RESPONSIBLE INDIVIDUAL HE HELIN		22b. TELEPHONE (include Area Code) 202 767 0471	22c. OFFICE SYMBOL NA	

(cont) → The data indicate that the mass removal initiates an oblique expansion wave at the leading edge of the bleed zone, increasing the Mach number of the normal shock. The expansion wave intersects the shock, initiating a weak shear layer in the subsonic flow. The boundary layer thickness remains approximately constant over the bleed zone. The streamwise velocity at the perforated plate is high, close to the freestream velocity. The turbulence intensity downstream of the bleed zone is comparable to the intensity of the approach boundary layer, in contrast to uncontrolled interactions in which the turbulence intensity is greatly amplified. → (to field 18 over)

PREFACE

This final report describes a research program performed by the McDonnell Douglas Research Laboratories, St. Louis, Missouri, on the structure of normal-shock/turbulent-boundary-layer interactions modified by mass removal. The research was sponsored by the Air Force Office of Scientific Research, under Contract No. F49620-86-C-0063. The work was performed from 1 June 1987 to 28 February 1989 in the Flight Sciences Department, managed by Dr. R. J. Hakkinen. Co-investigators were M. Sajben, M. J. Morris, J. C. Kroutil and T. J. Bogar. The Technical Manager of the program was initially Dr. James D. Wilson, and, after 1 November 1987, Dr. Henry E. Helin, both of the Air Force Office of Scientific Research.

R. J. Hakkinen

R. J. Hakkinen
 Director-Research
 McDonnell Douglas Research Laboratories

J. O. Dimmock

J. O. Dimmock
 Staff Vice President, Research
 McDonnell Douglas Research Laboratories

Accession For	
NTIS GRA&I	<input checked="" type="checkbox"/>
DTIC TAB	<input type="checkbox"/>
Unannounced	<input type="checkbox"/>
Justification	
By _____	
Distribution/	
Availability Codes	
Dist	Avail and/or Special
A-1	



TABLE OF CONTENTS

Section	Page
1. INTRODUCTION.....	1
2. OBJECTIVES.....	3
3. DESCRIPTION OF EXPERIMENT.....	4
3.1 Experimental Model.....	4
3.2 Flexible Wall.....	6
3.3 Perforated Wall.....	9
4. DIAGNOSTIC METHODS.....	13
5. CHARACTERIZATION OF MASS REMOVAL.....	15
6. RESULTS.....	18
6.1 Test Conditions.....	18
6.2 Qualitative Description of Flow.....	18
6.3 Time-Mean Data	22
6.4 Turbulence Quantities.....	37
7. SUMMARY AND CONCLUSIONS.....	42
8. REFERENCES.....	45
APPENDIX: Effect of Wall Contour Change.....	46

LIST OF ILLUSTRATIONS

Figure	Page
1. Experimental apparatus for the study of shock/boundary-layer interaction with mass removal.....	4
2. Approach Mach number and Reynolds number based on momentum thickness for experimental investigations of two-dimensional, transonic shock/boundary-layer interactions.....	5
3. Spark schlieren photograph of $M_0=1.49$ shock/boundary-layer interaction over a solid wall, with no mass removal.....	6
4. Flexible wall.....	7
5. Flexible wall control mechanism during assembly.....	9
6. Model installed in test facility.....	10
7. Details of perforated plate and removable panel.....	12
8. Details of orifice used for surface pressure measurements on the perforated wall.....	14
9. Approach velocity profile at $x=-4.44$ cm.....	19
10. Wave patterns induced by suction.....	21
11a. Flow property distribution in bleed zone for flow A.....	23
11b. Flow property distribution in bleed zone for flow B.....	24
12. Wall pressure distribution without and with mass removal.....	25
13. Contours of u/a^* in three cross-sectional planes, illustrating evolution of three-dimensional features of flow A.....	26
14. Contours of u/a^* in three cross-sectional planes, illustrating evolution of three-dimensional features of flow B.....	27
15. Streamwise distribution of u-velocity component at boundary-layer edge.....	29
16. Streamwise distribution of boundary layer thickness.....	29
17. Profiles of u-velocity component, normalized by the edge velocity.....	31
18. Profiles of u-velocity component over the bleed zone, at densely spaced x-locations.....	32

LIST OF ILLUSTRATIONS

Figure	Page
19. Streamwise distributions of u-velocity component at fixed distances from wall over bleed zone.....	33
20. Streamwise distributions of v-velocity component at fixed distances from wall.....	34
21a. Contours of $u/a^* = \text{constant}$ near the shock, for both flows.....	35
21b. Contours of $u/a^* = \text{constant}$ for $9 \text{ cm} < (x-x_0) < 18 \text{ cm}$, for both flows.....	36
22. Contours of $v/a^* = \text{constant}$ near the shock, for both flows.....	37
23a. Contours of $\hat{u}/a^* = \text{constant}$ near the shock, for both flows.....	38
23b. Contours of \hat{u}/a^* for $9 \text{ cm} < (x-x_0) < 18 \text{ cm}$, for both flows....	39
24. Contours of \hat{v}/a^* near the shock, for both flows.....	40
25. Contours of $-\overline{u'v'}/a^{*2}$ near the shock, for both flows.....	41
A-1. Effect of wall contour change on topwall pressure distribution (Flow B).....	46

LIST OF TABLES

Table	Page
1. Bottomwall contour coordinates.....	8
2. Bleed system information.....	11
3. Approach velocity profile.....	20

1. INTRODUCTION

Normal-shock/turbulent-boundary-layer interactions are dominant features of supersonic inlet flows. Such interactions significantly influence the time-mean and the dynamic characteristics of the subsonic flow following the shock.

A sustained adverse pressure gradient is invariably present in the final, subsonic region of supersonic inlet flowfields. This feature magnifies the adverse effect of the original interaction: the boundary-layer growth rate is much greater than that typically found in interactions followed by a constant-pressure region.¹ In zero-pressure-gradient flows, the separation bubble length is scaled by the boundary-layer thickness, whereas in adverse-pressure-gradient flows the bubble may grow to dimensions comparable to several duct heights.^{2,3}

For supersonic aircraft inlets substantial mass removal (bleed) is used almost invariably to control these undesirable effects. As much as 6-8% of the total mass flow may be removed.⁴ The inlet performance is usually improved by this method, but the gain is offset by several adverse consequences. The bleed flow, re-injected into the freestream, represents a momentum-deficit and therefore increases drag. The external drag is also increased because the inlet must be larger to deliver the required engine flow plus the bleed flow. Use of larger inlets also increases aircraft weight. The studies required to define the best compromise between inlet efficiency, drag, and weight are currently based on purely empirical information and require costly confirmation by model testing.

Decelerating subsonic flow and substantial mass removal are invariably present features of inlet flows, yet few past experimental investigations incorporated these elements in the configurations studied. Both of these features are capable of substantially modifying the flowfield; therefore, the applicability of the current information about shock-boundary-layer interactions to supersonic inlets is questionable.

A number of experimental investigations dealing with oblique-shock/turbulent-boundary-layer interactions affected by suction have been reported.^{5,6} In contrast, there seems to be no detailed experimental information available on the effects of mass removal on normal-shock/turbulent-boundary-layer interaction. There are studies of the performance

of various inlets equipped with bleed systems, but such studies do not include enough flowfield information to allow insight into the physical processes associated with mass removal.

The goal of the present investigation is to extend the experimental database relevant to normal-shock/boundary-layer interactions by studying flows with mass removal from a turbulent boundary layer in the presence of a post-shock, subsonic deceleration.

Mass removal has a twofold effect on the flow. The favorable effect is the elimination of the lowest energy portion of the boundary layer, which helps the flow to negotiate the adverse pressure gradient further downstream. An undesirable side effect is that the suction deflects the streamlines towards the wall, causing them to diverge. In a subsonic flow, diverging streamlines represent deceleration and a steepening of the already adverse pressure gradient. In a supersonic flow, diverging streamlines are associated with an accelerating flow and a stronger shock. The influence of suction on the mean flow thus encourages the tendency for separation at any speed. In a successful mass-removal system, the two opposing influences produce a net improvement.

To assess the contributions from these two mechanisms, it appeared desirable to control the streamwise pressure distributions in the subsonic region of the channel. A flexible wall was developed in this program to achieve this capability.

2. OBJECTIVES

The work statement of the contract is the following:

- a. Modify an existing experimental flow channel, designed at MDRL for the study of shock/boundary-layer interactions, by incorporating a flexible bottom wall. The wall shape will be adjustable by mechanical jacks.
- b. Impose at least two streamwise distributions of mass removal on the top wall and adjust the bottomwall configuration to obtain the same pressure distribution for each case. Obtain detailed wall-pressure and velocity distribution measurements, distributions of removed mass flow, and integral parameters for each case.

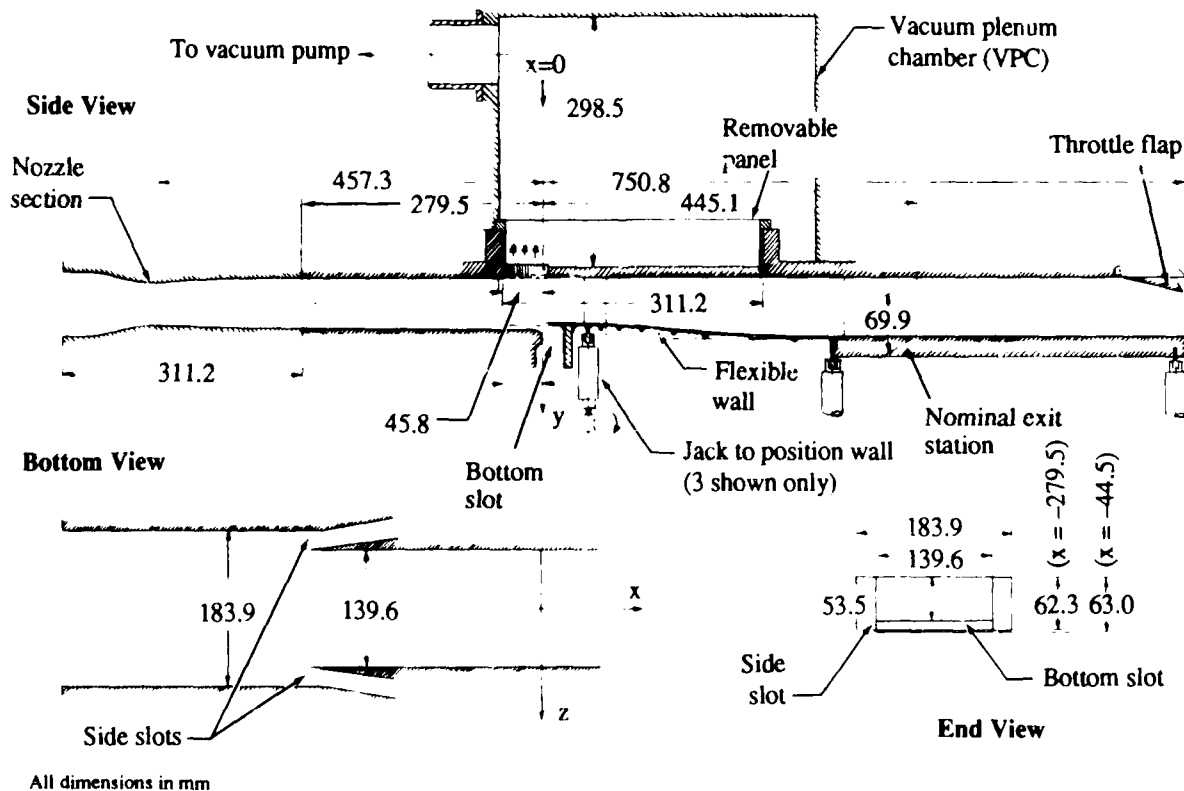
3. DESCRIPTION OF EXPERIMENT

3.1 Experimental Model

This program utilized experimental equipment developed earlier for the study of shock/boundary-layer interactions (SBLI) under a McDonnell Douglas Corporation-sponsored IRAD program. The program and the apparatus are described in detail elsewhere.⁷ This model, illustrated in Fig. 1, was modified for the present study.

The model generates a uniform, nominally steady supersonic flow at a Mach number of 1.49. The interaction of interest occurs on the flat, top wall of the device.

The bottom wall incorporates a scoop-type suction slot through which the bottomwall boundary layer is removed. The lip of this slot also serves to hold the shock stationary. The sidewall boundary layers are also removed several channel heights upstream of the shock. Only the topwall-boundary



89-222-178

Figure 1. Experimental apparatus for the study of shock/boundary layer interaction with mass removal. Removable top panel accepts perforated segments of arbitrary configuration. Flexible bottom wall controls streamwise pressure gradient.

layer is allowed to grow without interruption. As a result, the top layer accounts for 63% of the total displacement area at the shock location, including all four sides of the channel. Without the three suction slots, the top-layer contribution would be less than 36%. It is expected that the thick, topwall boundary layer exerts a dominant influence over the post-shock flow.

The channel diverges downstream of the shock, subjecting the post-shock boundary layer to an adverse pressure gradient. The exit-to-approach area ratio is 1.302, the length-to-height ratio of the divergent portion is 4.5, and the maximum wall angle to the horizontal is five degrees. The channel is terminated by a two-dimensional flap mounted on the top wall, and is used to control the exit area and thereby the location of the normal shock inside the duct. The flow is choked at the flap-controlled exit station.

The nominal stagnation pressure in the plenum chamber preceding the model was typically 224 kPa and the nominal stagnation temperature was 300 K.

The Reynolds number based on the momentum thickness of the boundary layer just in front of the shock is 14,600, which places this experiment in the middle of the Reynolds-number range for past shock/boundary-layer interaction experiments (Fig. 2). The ratio of the approach-boundary-layer displacement thickness to the channel height at the shock is 1.4%. This ratio,

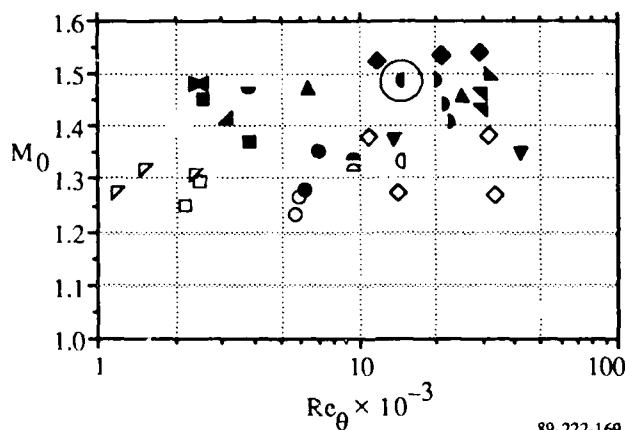


Figure 2. Approach Mach number and Reynolds number based on momentum thickness for experimental investigations of two-dimensional, transonic shock/boundary-layer interactions. Open symbols indicate attached flows, full symbols denote shock-induced separation. Sources of data are given in Ref. 7. Circled symbol denotes present study.

also known as blockage, is generally well below 1% for most past experiments, but may be well above 1% in inlets designed for high supersonic and hypersonic speeds.

The manipulation of the sidewall and bottomwall boundary layers, together with the large width-to-height ratio of the channel cross section ($=3.2$) ensure a close approximation to a two-dimensional flow.

A spark schlieren photograph of the uncontrolled (no mass removal, "unbled") flowfield is shown as Fig. 3. The boundary layer is separated by the shock, creating a characteristic lambda shock-pattern.

The experiments of Reference 7 were performed with a fixed bottom wall. For the purposes of the present study, this wall was replaced by a flexible one, to be described in the next section.

3.2 Flexible Wall

Figure 4 illustrates the side view of the flexible portion of the wall in its undeflected state. The wall coordinates can be set at 11 points (nodes). The first node is fixed and the wall slope is zero, i.e., the wall has a horizontal tangent at its beginning. The last two nodes are connected by an airtight, rigid wall, which was kept horizontal by moving the two end-nodes simultaneously. The distances between the nodes vary in approximate proportionality to the expected radii of wall-contour curvatures, and the wall thicknesses follow the same trend.

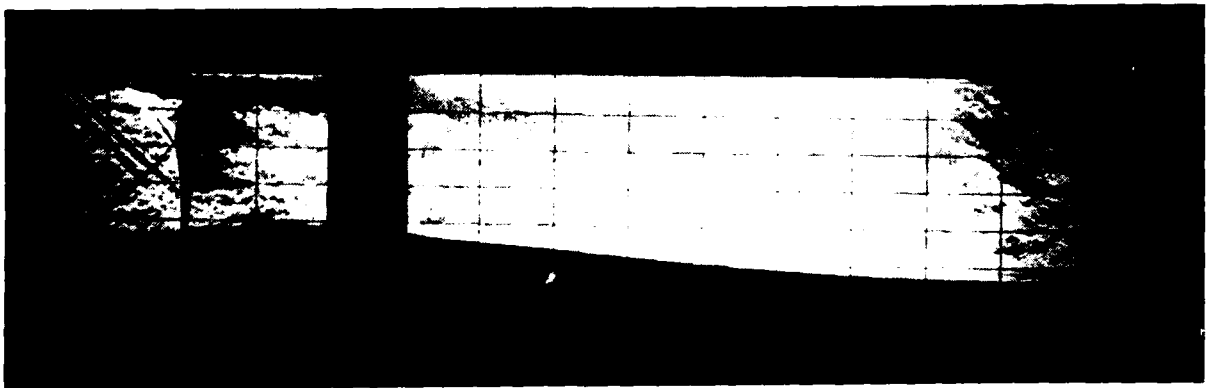
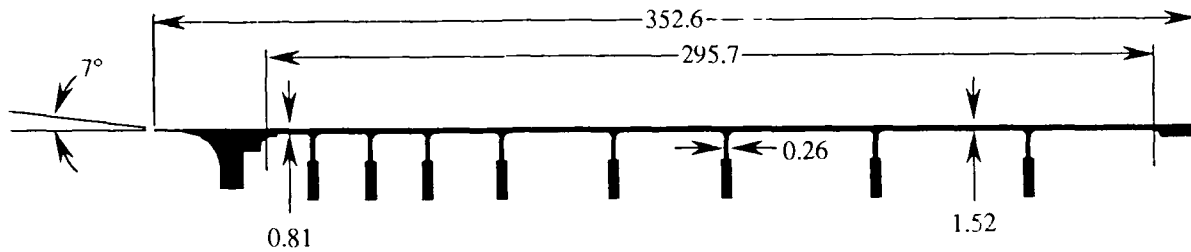


Figure 3. Spark schlieren photograph of $M_0 = 1.49$ shock/boundary-layer interaction over a solid wall, with no mass removal. Lambda pattern indicates shock-induced separation. Superimposed grid dimensions are 25.4 mm by 12.7 mm.



All dimensions in mm

89-222-170

Figure 4. Flexible wall. Integrally machined tabs connect to positioning jacks, also provide lateral stiffening. Spacing between tabs and wall thickness vary to accommodate wall curvatures required.

The nodes are set with the aid of mechanical jacks, attached to the integrally machined tabs at the node locations. The tabs are sufficiently thin and flexible to accommodate the deformations required at the attachment points. Each node can be positioned by a mechanical jack with a 0.016-mm resolution. A special caliper was available for independent measurement of the actual channel geometry (height vs. axial distance) with ± 0.03 mm accuracy.

A desired channel shape was set by a multistep procedure. The actual shape (that happened to exist after initial assembly was completed) was initially determined using the calipers. The counter settings at all nodes were also recorded. Comparison of the actual shape with the desired one yielded the necessary channel-height changes for each node. The node jacks were then successively adjusted to the desired shape. The final shape was again checked with the calipers. The measured wall coordinates (y_w) are given in Table 1; the coordinate system used is shown in Fig. 1. The $x=0$ location is defined as the leading edge of the shock holder.

The thickness of the wall was dictated by the need to minimize the deflections attributable to the pressure differentials: the wall was not to bulge either laterally or in the streamwise direction. The jack attachment tabs served as lateral stiffeners. The minimum thicknesses, combined with the desired wall-curvatures, resulted in relatively high jack forces (up to 1000 N) that threatened to buckle the tabs. The bending stresses in the wall were also considerable. Because of the high gear-ratio of the jacks, there was a potential of imposing displacements large enough to permanently

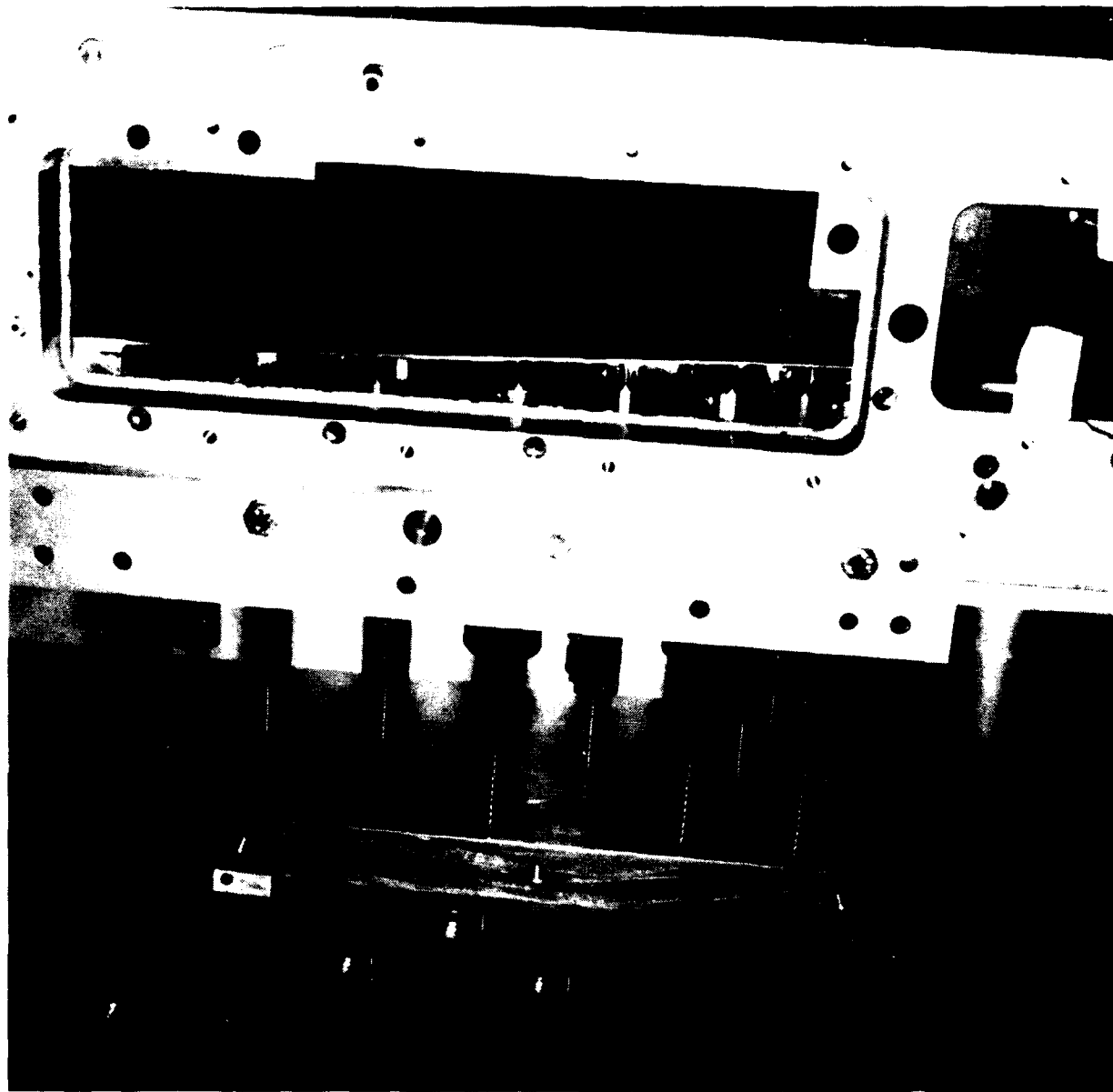
Table 1. Bottomwall contour coordinates.

x (mm)	y _w (mm)
0.0	53.52
	Straight line
31.7	53.52
38.1	53.53
44.4	53.59
50.8	53.72
57.1	53.95
63.5	54.30
69.8	54.79
76.2	55.30
82.5	55.86
	Straight line
146.0	61.57
152.4	62.18
158.7	62.81
165.1	63.27
171.4	63.96
177.8	64.52
184.1	65.07
190.5	65.68
196.8	66.22
203.2	66.85
209.5	67.44
215.9	68.00
222.2	68.43
228.6	68.83
234.9	69.16
241.3	69.42
247.6	69.60
254.0	69.75
260.3	69.85
	Straight line
727.7	69.85

89-222-167

damage the wall. To prevent this eventuality, a computer code was written to calculate, for any prescribed set of jack positions, the jack forces, the bending stresses, and the wall coordinates. This code was used in an interactive manner to arrive at a sequence of jack settings that permitted a transition from one wall shape to another, without exceeding any stress limitation.

Figure 5 is a photograph of the wall and the associated mechanisms during assembly, and Fig. 6 shows the model installed in the test cell. The



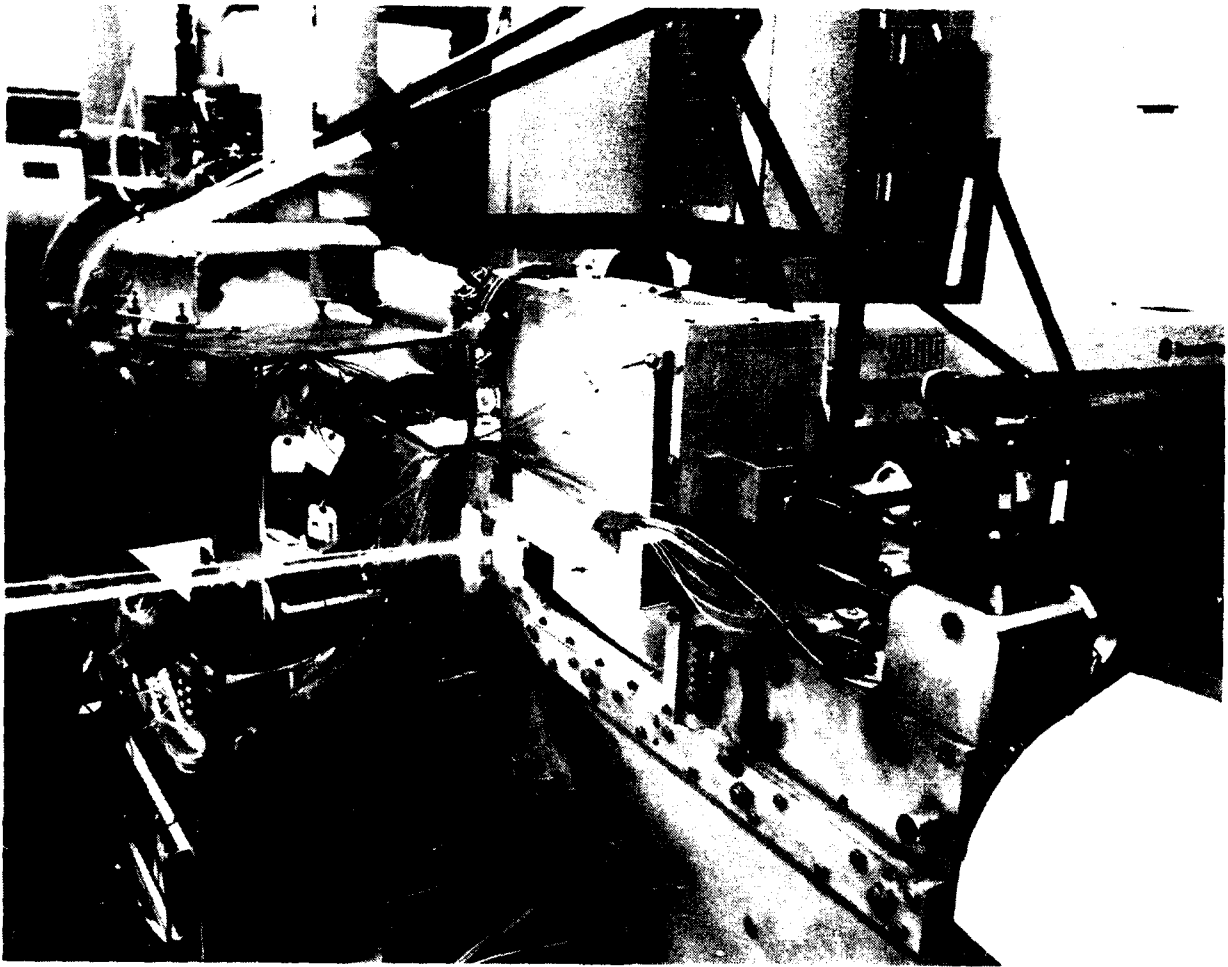
89-222-171

Figure 5. Flexible wall control mechanism during assembly.

flexible-wall mechanism and the procedures developed for its use worked satisfactorily.

3.3 Perforated Wall

Since the investigation was intended to generate data suitable for code validation, the perforated surface was designed to approximate continuous mass removal, a boundary condition usually employed in theoretical models.



89-222-183

Figure 6. Model installed in test facility. Bracket structure supports the LDV receiving optics. Box-like enclosure is vacuum plenum chamber covering perforated plate.

This implies that the length scale of the porosity (e.g., spacing between holes) should be much shorter than the boundary-layer thickness. This requirement conflicts with conditions present in operational inlets, where the size of the perforations is usually on the order of the boundary-layer thickness.

The two bleed-configurations used in these experiments both employed perforated plates as the wall surface material. Configuration A used a 7% open-area fraction while configuration B used 14%. The respective flows will be designated as flow A and flow B. The open-area fraction was the principal factor controlling the rate of removed mass flow. The perforations were small and closely spaced (50 and 31 perforations per cm for

configurations A and B, respectively). Details of the plates are given in Table 2. The downstream edge of the plate was at the same axial location as the shock-holder ($x=0$), for both cases. The perforated surface spanned the full channel width. Since the open-area fractions were low, most of the surface had the original smoothness of the metal and surface roughness was unlikely to have had much influence on the resulting flowfield.

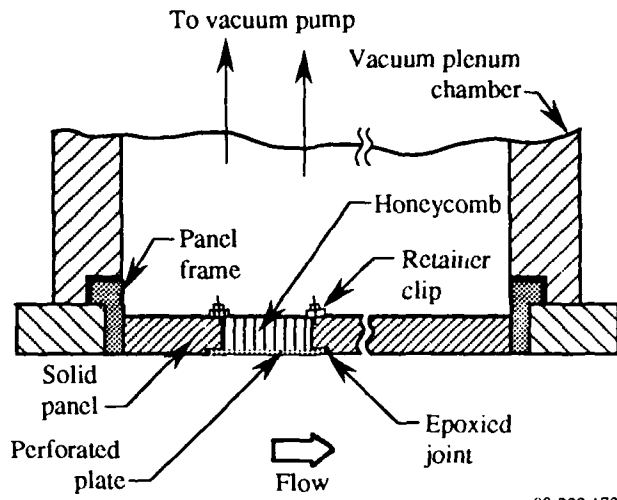
To provide the mechanical strength necessary to withstand the 40- to 80-kPa pressure differential expected across the plate, it was backed by a honeycomb structure.

Figure 7 shows the design of the removable wall panel that included a perforated segment. As shown in Fig. 1, a large vacuum plenum chamber (VPC) covered the perforated plate assembly. The plenum was connected to a large-capacity vacuum system ($250 \text{ m}^3/\text{s}$), capable of keeping the VPC pressure sufficiently low to choke the flow at the perforations.

Table 2. Bleed system information.

Dimensions (Length dimensions in mm)	A	B	
Open-area fraction	0.07 ± 0.01	0.135 ± 0.01	
Hole diameter	0.05	0.13	
Hole spacing	0.20	0.32	
Wall thickness	0.127	0.064	
Location of bleed zone leading edge	-39	-39	
Streamwise length of bleed zone	39	39	
Performance			
Average normalized mass flow $\bar{\sigma}$	0.025	0.080	
Bleed flow/boundary layer flow	S_{δ^*}	0.97	3.01
	S_{δ}	0.231	0.740
Bleed flow/total flow in channel	S_A	0.0060	0.019

89 222-207



89-222-172

Figure 7. Details of perforated plate and removable panel.

4. DIAGNOSTIC METHODS

Noise and safety considerations did not allow access to the test cell during runs, but the flow could be observed using a black-and-white video camera incorporated into the laboratory schlieren system. The preliminary exploration of the flowfields made intensive use of this camera, both in real time and also by recording representative events on video tape. In particular, the unsteadiness of the flow, which is always an issue in transonic internal flows, could be readily documented.

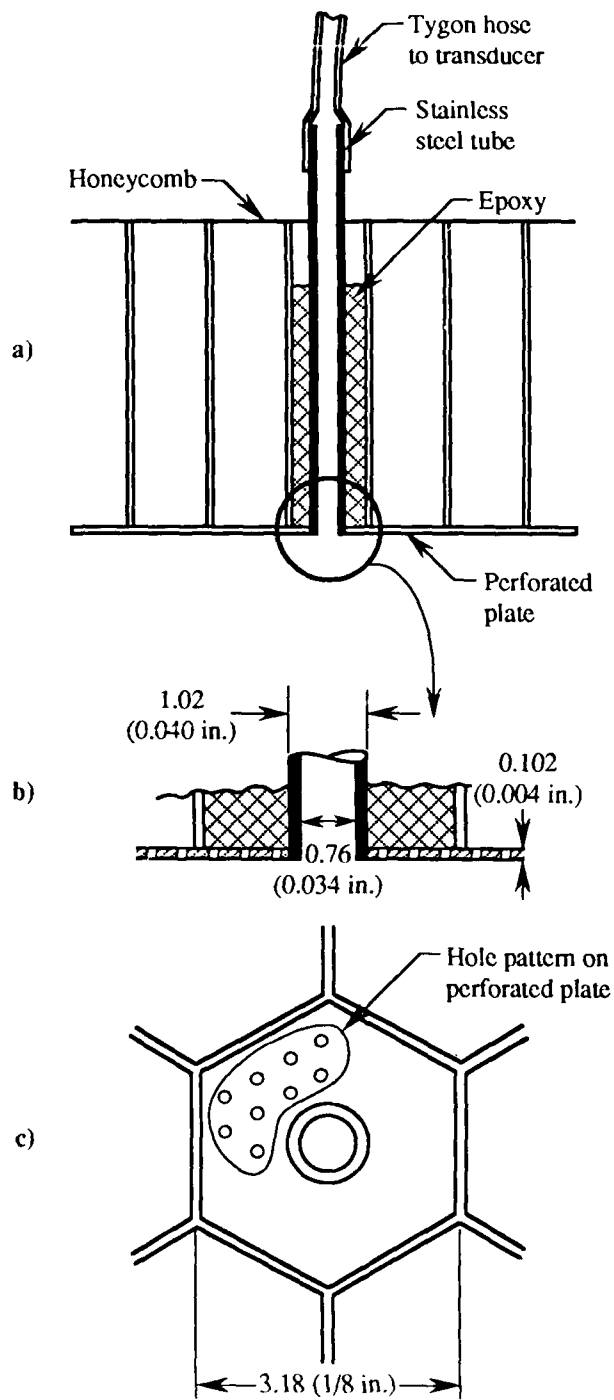
One shortcoming of the video camera was the low frame rate (30 frames/s), which made it necessary to complement the visual data with a high-speed movie camera (5000 frames/s) for selected flow conditions.

Surface-pressure distributions were measured by a 96-port system capable of measuring instantaneous pressure distributions.

The determination of the surface pressure over the perforated plate was not a trivial problem. The solution arrived at, after some experimentation, is illustrated in Fig. 8. A small-pressure orifice (0.76-mm diam, much larger than the plate perforations) was connected to a stainless steel tube on the outside of the plate. The tube was epoxy-cast into a single honeycomb cell and the epoxy surface was bonded to the perforated plate by an adhesive. Each steel tube was then connected to a transducer via a small-diameter tygon tube. This arrangement blocks the bleed flow through the cell it occupies and thus involves a slight spatial disturbance of the flow pattern. However, the error is of the order of σ^2 and is therefore quite small. (See Section 5 for the definition of σ .)

The mainstay of the diagnostic effort was a two-component laser-Doppler velocimeter (LDV) with a 5-W argon laser and Dantec optics. The Doppler bursts were analyzed with TSI counters, with a master interface allowing the acquisition of coincident data. The system and the data-acquisition procedures are described in detail in Reference 7.

Data were acquired over a grid comprising 24 streamwise stations and 30 or more points per station.



89-222-173

Figure 8. Details of orifice used for surface pressure measurements on the perforated wall. (b) and (c) are enlarged illustrations of portion circled on (a). Perforated plate shown is for case A.

5. CHARACTERIZATION OF MASS REMOVAL

The operation of a given bleed system may be characterized in several ways.

The local suction rate will be normalized by the mass flux at the boundary-layer edge, at the x -location where the influence of the suction is first detected. With this location designated by the subscript $(\)_b$, the normalized suction rate is defined by

$$\sigma = - \frac{\rho_w v_w}{(\rho_e u_e)_b} \quad (1)$$

where ρ is density, u is the x -component and v the y -component of the velocity vector. The subscript w refers to the wall surface, and e to the boundary-layer edge.

The bleed zone has an upstream influence through the subsonic portion of the approaching boundary layer, therefore the location x_b is several boundary-layer thicknesses upstream of the leading edge of the bleed zone. Note that in Eq. (1) the numerator is a function of x , but the denominator is a constant for the flow.

The experimental determination of $\sigma(x)$ requires considerable effort, while the measurement of the total removed-mass-flow rate may be much easier. The mass flow removed (per unit span) is given by

$$w_b = \int_0^{\ell} \rho_w v_w dx \quad (2)$$

where ℓ is the streamwise length of the bleed zone. Using w_b , the average value of σ is obtained as

$$\bar{\sigma} = \frac{1}{\ell} \int_0^{\ell} \sigma dx = \frac{1}{\ell(\rho_e u_e)_b} \int_0^{\ell} \rho_w v_w dx = \frac{w_b}{\ell(\rho_e u_e)_b} \quad (3)$$

Other integral parameters may be obtained by referencing the removed mass flow to various characteristic values of mass flow. One obvious choice

is the boundary-layer mass flow, obtained by integrating the mass-flow profile from the wall to the boundary-layer edge:

$$w_{\delta} = \int_0^{\ell} \rho u dy = \rho_e u_e (\delta - \delta^*) \quad (4)$$

where δ is the thickness defined by the location of the boundary-layer edge and δ^* is the displacement thickness. This choice of reference flow rate yields the fraction of the boundary-layer flow removed by suction:

$$S_{\delta} = \frac{w_b}{[\rho_e u_e (\delta - \delta^*)]_b} \quad (5)$$

A disadvantage of this parameter is that the measurement of δ is difficult and inaccurate, therefore its use may lead to erratic results. The displacement thickness, δ^* , is generally more accurate and a more reliable parameter results if the quantity $(\delta - \delta^*)$ in Eq. (5) is replaced by δ^* , leading to

$$S_{\delta^*} = \frac{w_b}{[\rho_e u_e \delta^*]_b} \quad (6)$$

Note that δ is generally much greater than δ^* , making the numerical values of S_{δ} and S_{δ^*} quite different.

In the design of propulsion systems, the total channel mass flow is a natural reference quantity whose use results in the parameter

$$S_A = \frac{w_b}{w_A} \quad (7)$$

where the subscript A refers to the full cross section of the channel.

The parameters discussed in this section are not equivalent: none of the above parameters define any other uniquely. However, $\bar{\sigma}$ and S_{δ^*} are related as follows:

$$\frac{\bar{\sigma}}{S_{\delta^*}} = \left(\frac{\delta^*}{\ell} \right) \quad (8)$$

The displacement area defined by the boundary layer around the entire perimeter and divided by the channel cross-section area is commonly referred to as the blockage, B. If suction is applied uniformly around the perimeter, then the parameters S_A and S_{δ^*} are related according to the equation:

$$\frac{S_A}{S_{\delta^*}} = B \quad (9)$$

where B refers to conditions just upstream of the bleed zone.

Each of the four integral parameters introduced has its own utility, depending on the context of the particular application. For the purposes of this study, $\bar{\sigma}$ and S_{δ^*} are the most relevant.

6. RESULTS

6.1 Test Conditions

The properties of the approach freestream were $M = 1.49$ and unit $Re = 2.1 \times 10^6$ per meter. Stagnation pressure in the plenum chamber was held constant at 224 kPa and the nominal stagnation temperature was 300 K.

Properties of the approach boundary layer are illustrated in Fig. 9 and tabulated in Table 3. The profile is a reasonably good approximation to a fully developed, turbulent boundary layer at zero pressure gradient, and, as illustrated in Fig. 9b, can be fitted well by a logarithmic wake profile.

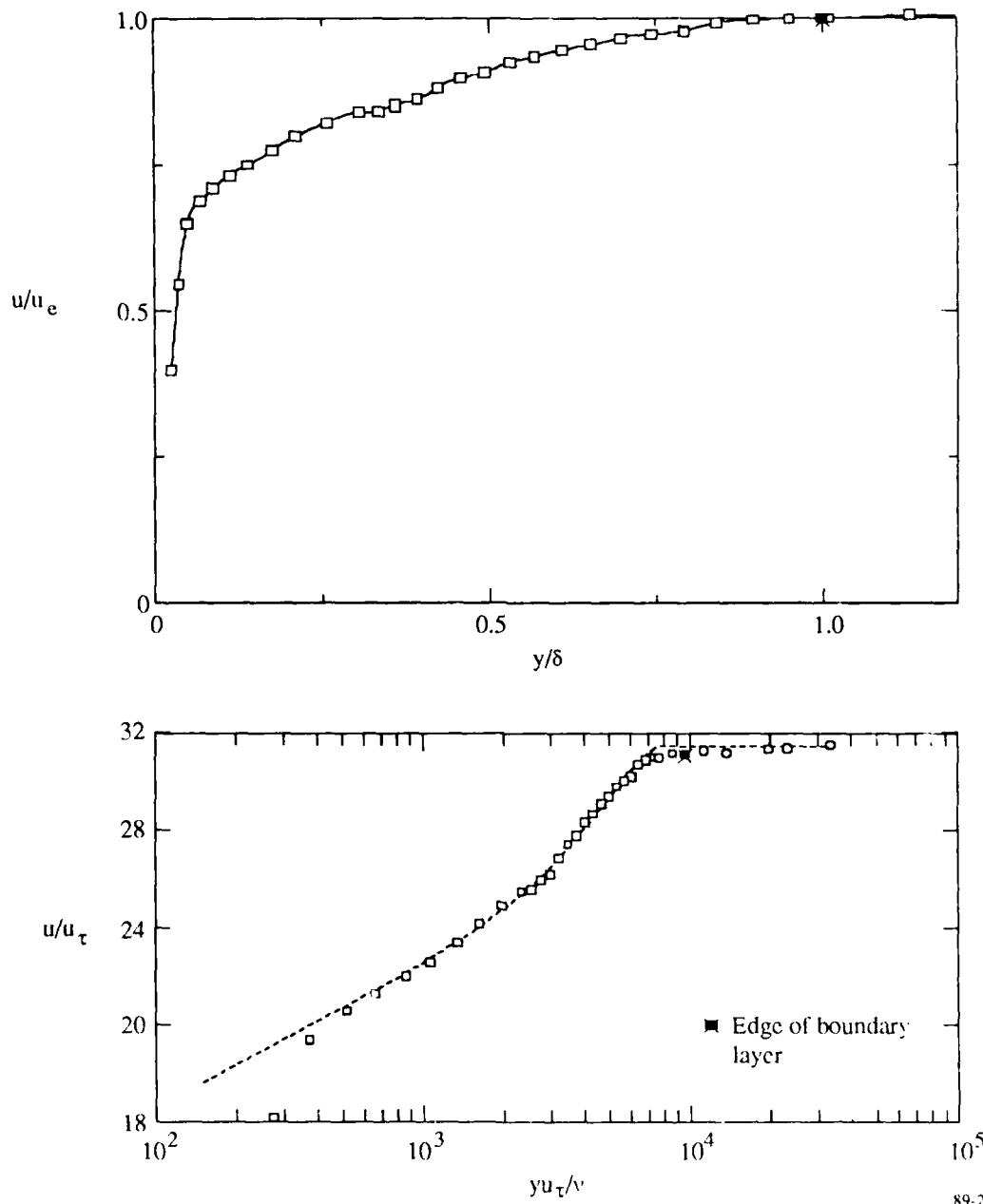
Contrary to the original plans, the wall contours were kept the same for both flows investigated. This change was prompted by the preliminary findings. The results showed that mass removal alters the pressure distribution in such a way that no wall shape can lead to identical wall pressure distributions for bled and unbled cases. Given this fact, the best alternate approach was to keep the geometrical configuration (including the location and length of the bleed zone) fixed and vary only the amount of mass removed.

The nominal pressure in the vacuum plenum chamber was 33 kPa absolute for flow A and 38 kPa absolute for flow B. The nominal static pressure in the supersonic approach flow was ~ 62 kPa, such that the pressure ratio across the perforated wall was 0.53. This ratio was sufficiently small to ensure essentially choked flow through the individual perforations.

6.2 Qualitative Description of the Flow

Figures 10a and 10b are schlieren photographs of flows A and B. Figure 10c is an interpretive sketch, highlighting the principal elements of the pattern.

The sketch of Fig. 10c shows that the bleed flow initiates a Prandtl-Meyer expansion at the upstream edge of the bleed zone (point A). The expansion deflects the flow towards the wall, the angle of deflection being approximately equal to $\bar{\sigma}$ (radians). The pressure decreases and the Mach number increases across the expansion fan. The expansion fan intersects the shock at point B, initiating a very weak vortex sheet (velocity discontinuity, or slip line). The shock segment from A to the opposite wall is inclined to allow the shock to be attached at the shock holder, point C.



89-222-174

Figure 9. Approach velocity profile at $x = -4.44$ cm. (a) Normalized by values at the edge of the layer, (b) normalized by friction velocity. Dashed line is a Coles wall-wake profile for $C_f = 0.0023$ and $\pi = 0.8$.

Table 3. Approach velocity profile.

$$x = x_0 = -4.45 \text{ cm}$$

$$\delta = 0.528 \text{ cm}$$

$$u_c/a^* = 1.358$$

y/δ	u/u_c
1.000	1.000
0.950	1.006
0.897	1.003
0.843	0.998
0.793	0.983
0.744	0.978
0.699	0.971
0.653	0.960
0.612	0.951
0.570	0.939
0.532	0.928
0.494	0.913
0.458	0.902
0.424	0.886
0.394	0.866
0.362	0.858
0.335	0.846
0.307	0.844
0.259	0.826
0.212	0.803
0.176	0.779
0.140	0.754

89-222-181

Due to the expansion-increased Mach number, the shock losses are slightly greater than what they would be without bleed.

The spark schlieren photos (Fig. 10a,b) show that the expansion fan is, in reality, quite broad. The suction has an upstream influence through the subsonic part of the boundary layer and it begins to affect the boundary layer upstream of the bleed zone. The broad expansion fan, when intersecting the shock, creates a thick shear layer instead of an infinitesimally thin slip-surface. The velocity change across the shear layer is very small and the presence of the layer is barely detectable experimentally.

As will be shown shortly, the mass-flow distribution along the bleed zone is not uniform. This nonuniformity implies the presence of waves reflected from the porous surface and further complicates the supersonic portion of the flowfield.

High-speed schlieren movies show highly turbulent flow in the central, core-flow region where an inviscid flow exists in the unbled case. The most

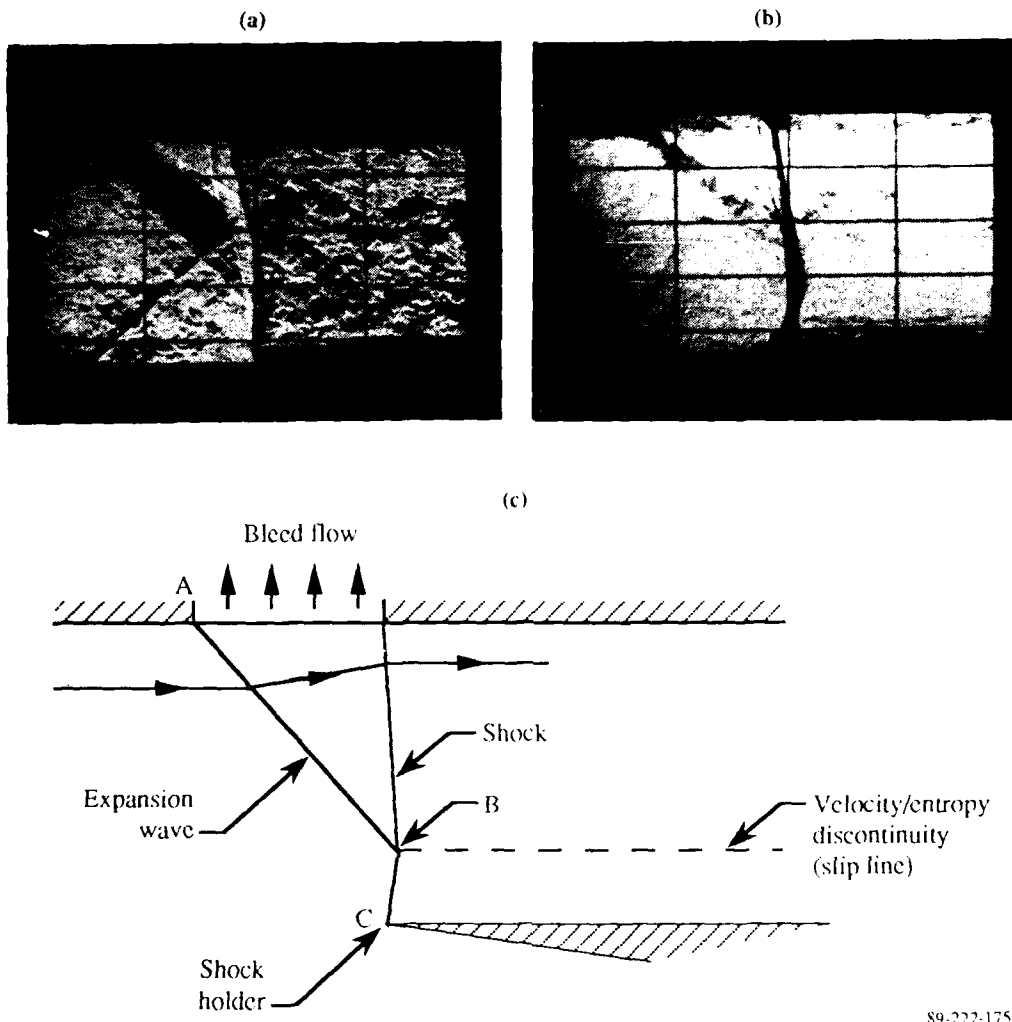


Figure 10. Wave patterns induced by suction. (a) Flow A. (b) Flow B. (c) Interpretive sketch.

likely explanation is that the sidewall boundary layers, which were probably attached without suction, are separated by the extremely sharp pressure rise created by the mass removal.

The high-speed movies also indicate that the shock was not stationary with bleed: it oscillated randomly in the streamwise direction. The oscillations are not related to the vacuum system characteristics, since the perforations were choked. The fluctuations in shock position were unexpected because the shock was reasonably stationary without suction and mass removal was thought to exercise a stabilizing influence. The shock oscillations cover a streamwise range of approximately 4 mm in the no-suction case, 12 mm

in flow A, and 16 mm in flow B. The oscillations affected the LDV measurements in the vicinity of the shock adversely; the consequences will be discussed later.

6.3 Time-Mean Flow Data

The character of the flow is strongly affected by mass removal; thus, it is useful to discuss at first the data that relate directly to the bleed zone.

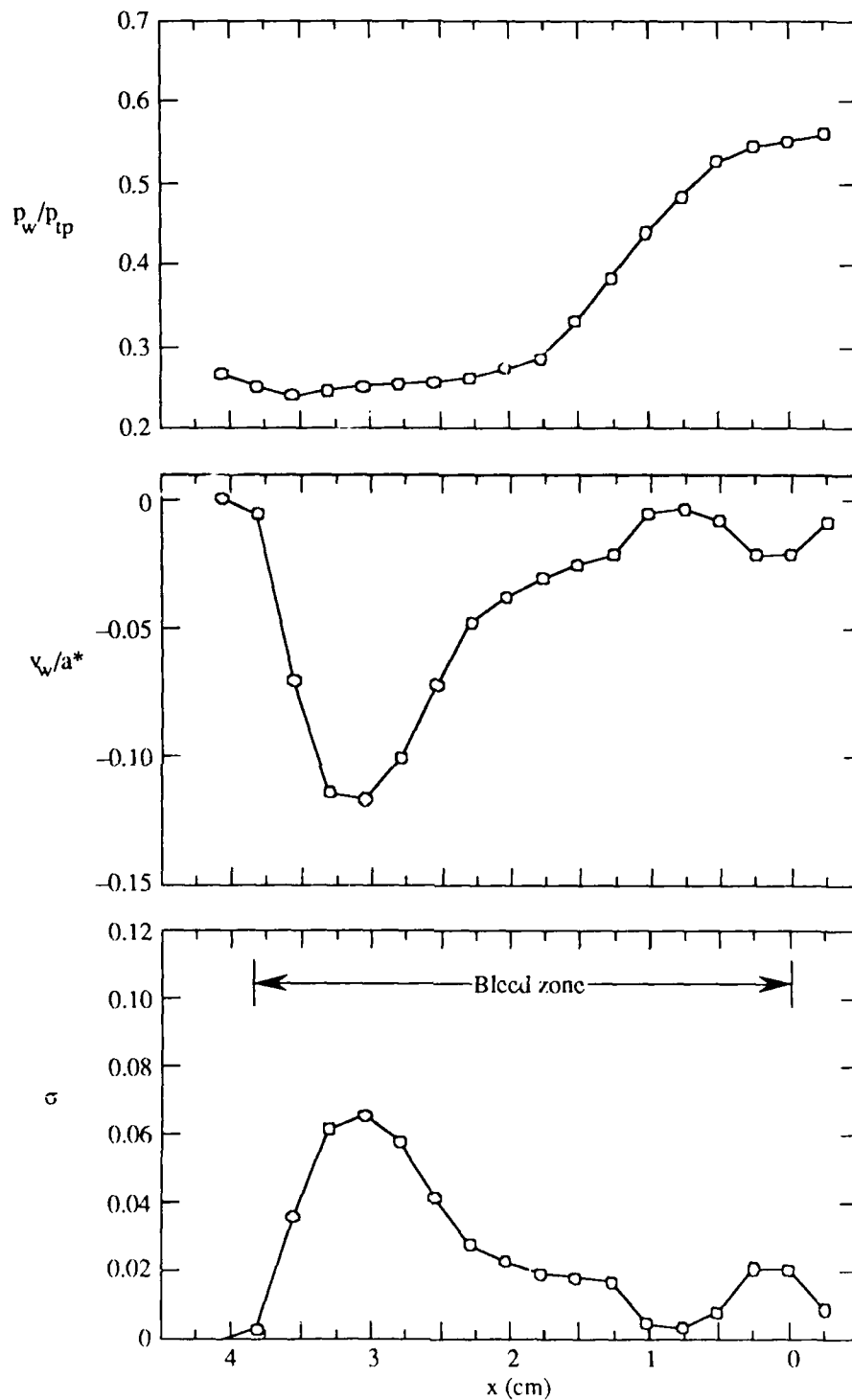
Figure 11 illustrates, for both cases, the streamwise distributions of the surface pressure, the velocity components, and the local suction rate $\sigma(x)$ over the bleed zone.

The velocities shown were measured by LDV at a distance of $y=0.25$ mm from the wall. The measurements, when repeated at several slightly higher y values, gave nearly identical distributions, indicating that extrapolation to the wall is valid and the distributions can be assumed to apply at $y=0$ as well. The surface pressures were determined using orifices illustrated in Fig. 8. The densities required to compute the parameter σ were determined from the static pressure, the total velocity magnitude, and the known stagnation temperature.

The v -component was expected to be greater in the subsonic region than in the supersonic portion of the bleed zone. The measurements do not confirm this expectation. In flow A, the velocity peaks early and shows a declining trend over most of the zone. In flow B, the distribution is reasonably uniform, although there is a distinct disturbance near the leading edge. The reasons for these features are not understood.

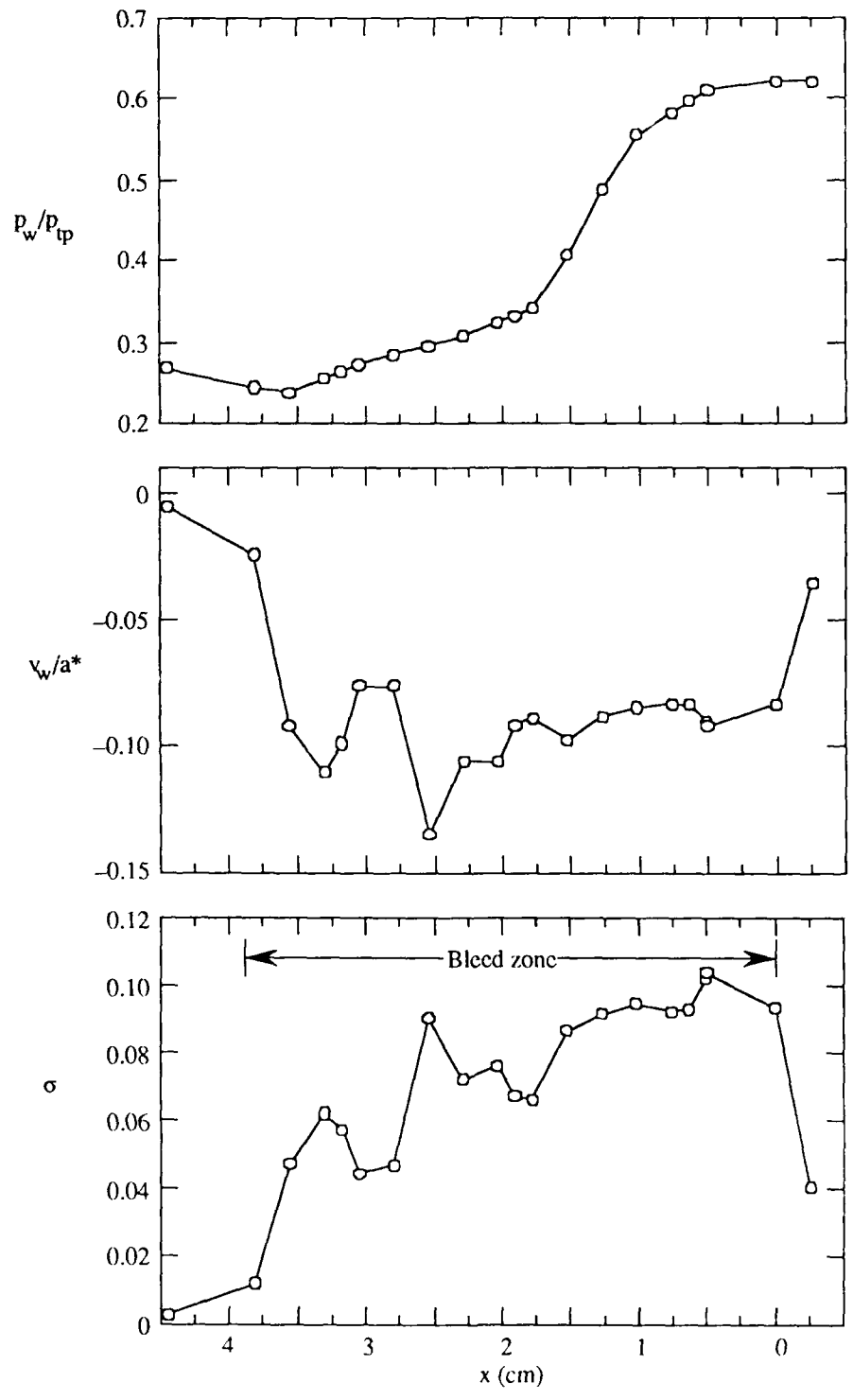
With the above information, it is possible to calculate all the parameters discussed in Section 5. The numerical values obtained are listed in Table 2. The substantial differences among the numbers indicate that careful parameter definition is essential, especially since no commonly accepted conventions seem to exist.

Figure 12 illustrates the top (interaction) wall surface-pressure distributions, without and with suction, over the entire length of the model. The distribution obtained with bleed shows a sharp initial drop before the shock: this drop is a consequence of the expansion fan described in the previous section. The pressure rise across the shock is very rapid and the



89-222-184

Figure 11a. Flow property distribution in bleed zone for flow A. From top to bottom: wall static pressure, vertical velocity component, normalized mass flow. Velocities measured at $y = 0.25$ mm.



89-222-185

Figure 11b. Flow property distribution in bleed zone for flow B. From top to bottom: wall static pressure, vertical velocity component, normalized mass flow. Velocities measured at $y = 0.25$ mm.

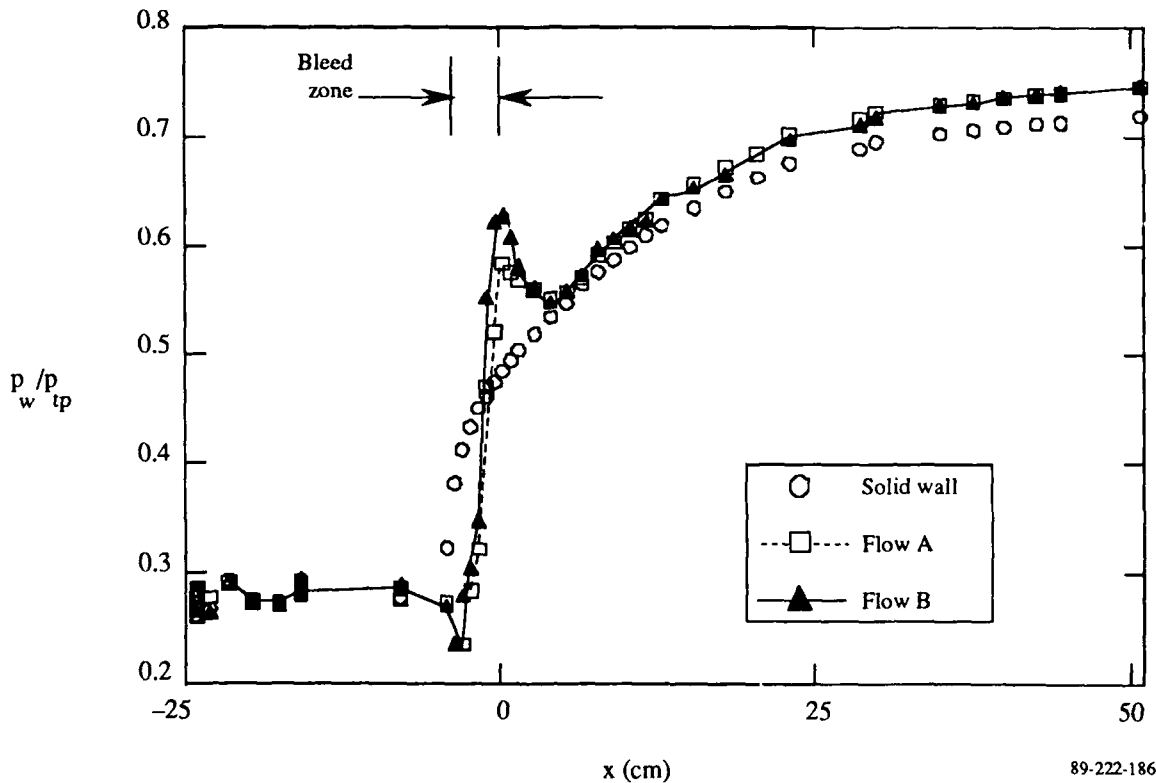
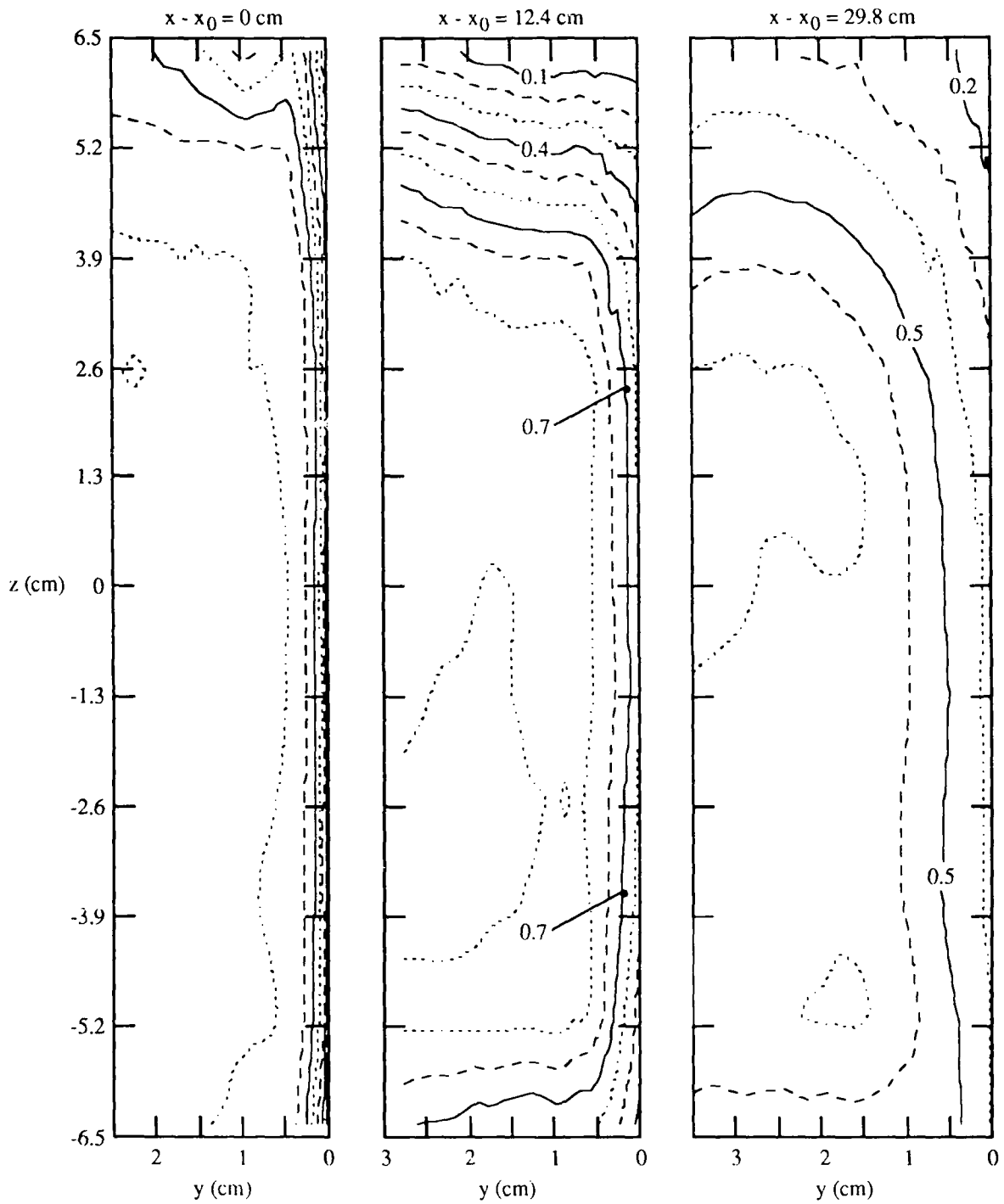


Figure 12. Wall pressure distribution without and with mass removal.

pressure reaches a sharp maximum that is only 6% less than the theoretically expected post-shock value for a normal shock.

After the shock, the pressure immediately drops again by as much as 12%. This pressure drop signals a subsonic acceleration which is probably induced by a decrease in the effective cross-sectional area. Such a decrease could be caused by a rapid growth of boundary layers immediately after the shock. It is possible that a substantial contribution to this growth is associated with the sidewall boundary layers. As mentioned in the previous section, it is likely that the rapid pressure rise across the shock causes the sidewall boundary layer to separate, which would account for a large increase of the displacement thickness on that wall.

The rapid growth of sidewall boundary layers is clear from the velocity measurements made at three streamwise stations, illustrated in Figs. 13 and 14. The stations are labeled with the streamwise distance from the first noticeable effect of suction, $x-x_0$, where $x_0 = -4.45$ cm. The two-dimensionality of flow deteriorates rapidly in the streamwise direction.



89-222-198

Figure 13. Contours of u/a^* in three cross sectional planes, illustrating evolution of three-dimensional features of flow A. Labels indicate distance from beginning of interaction ($x_0 = -4.45$ cm).

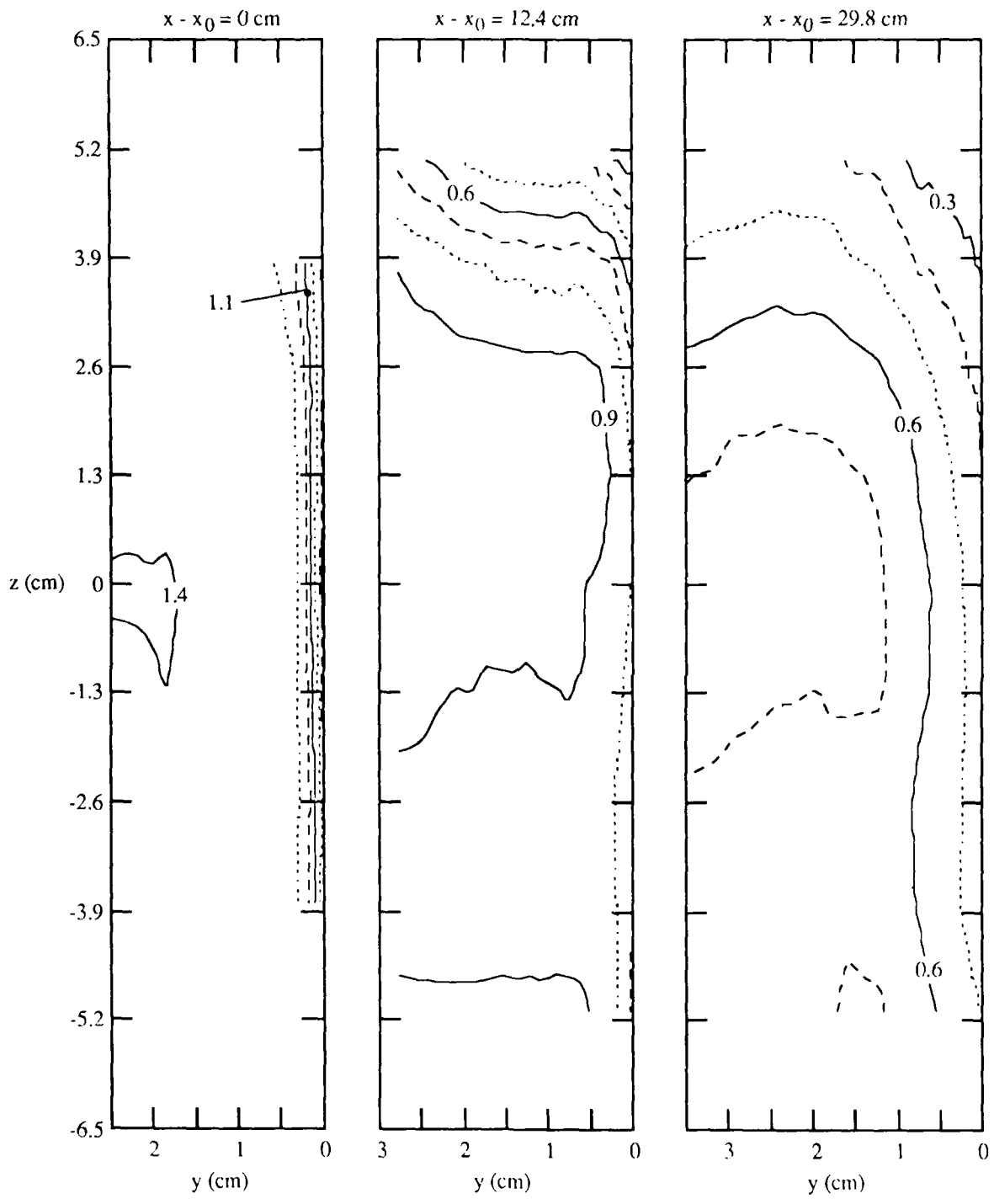


Figure 14. Contours of u/a^* in three cross sectional planes, illustrating evolution of three-dimensional features of flow B. Labels indicate distance from beginning of interaction ($x_0 = -4.45$ cm).

Flow A shows much more growth than the somewhat comparable Ref. 1 flow and Flow B, with a higher suction rate, clearly has the thickest sidewall layers of all three. The imposition of bleed on the top wall thus worsened the situation on the sidewalls: not only is the growth of the boundary layer greater, but the flow loses its symmetry as well.

The static pressure at the end of the diffuser is approximately 4% higher than the pressure with no suction, for both cases. This observation follows expectations: a lower mass flow rate corresponds to higher static pressure at a given stagnation condition. (The freestream stagnation pressure is not changed by the mass removal.)

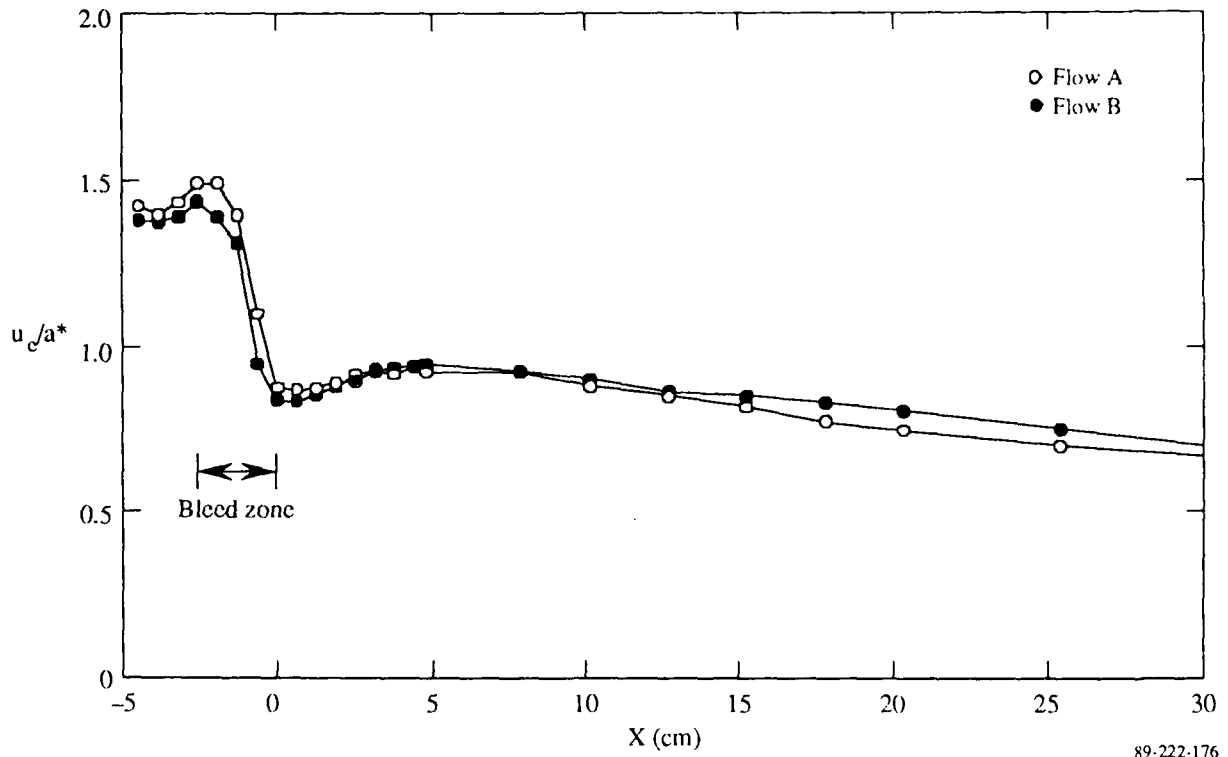
It is apparent from Fig. 12 that the pressure distributions created by bleed are qualitatively different from the distribution obtained with a solid wall. The differences are striking and highly localized near the shock. Modifications of the wall shape could affect the pressure distributions farther downstream in the diffuser section. However, no feasible change in wall shape would have an effect on the peculiar features of the pressure distribution in the vicinity of the shock. (Appendix A describes the results of a particular contour change).

The original approach to the problem of keeping the streamwise pressure-distribution constant proved unworkable and the alternate avenue of keeping the channel geometry constant was chosen instead. The two flows explored differ only in the wall porosity employed in the bleed zone (and therefore in the removed-mass-flow rate).

In the following, results for flows A and B will be presented side by side for easier comparison.

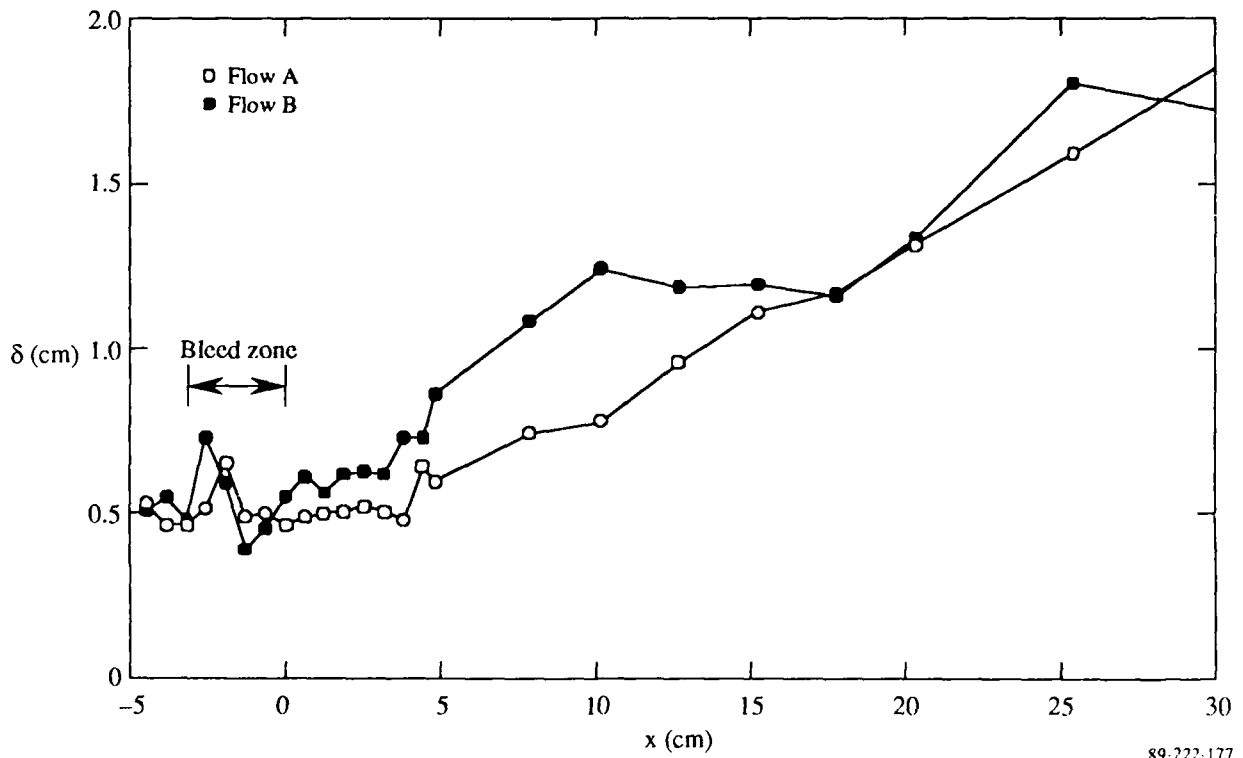
The streamwise distributions of the x-component of velocity at the boundary layer edge are shown in Fig. 15. The distributions are quite similar: both show the initial expansion, a rapid reduction across the shock and a post-shock acceleration--features also observable in the pressure distributions.

The streamwise distributions of the boundary-layer thickness are given in Fig. 16. These thicknesses represent the y-locations where the velocity reaches the freestream value. The determination of this location is subjective: the presence of expansion waves in the freestream obscures the boundary between the rotational and irrotational flow. This error is probably responsible for unexpected trend of data; flow B displays a thicker boundary



89-222-176

Figure 15. Streamwise distribution of u velocity component at boundary-layer edge.



89-222-177

Figure 16. Streamwise distribution of boundary layer thickness.

layer over most of the measurement region than flow A. Eventually, however, the boundary-layer thicknesses become nearly equal at $x \approx 30$ cm.

Figure 17 illustrates profiles of the x-component of the velocity for 15 streamwise stations, spanning a region from upstream of the interaction to the end of the divergent section. The boundary-layer thickness stays relatively constant over the bleed zone for both flows: mass removal appears to balance the entrainment at the outer edge. The velocity at the wall is much increased, but the edge of the profile stays at about the same distance from the wall. Downstream of the bleed zone, the profiles develop in a manner that closely resembles most other adverse-pressure-gradient flows.

Figure 18 shows 18 velocity profiles closely spaced within the bleed zone for flow A. These profiles confirm that the velocity profile varies little within the bleed zone.

Another way of characterizing the effect of suction is presented in Fig. 19 in the form of streamwise distributions of the x-velocity component, for fixed values of y.

At $y=0.025$ cm the suction-induced acceleration leads to a significant increase of velocity. The higher speed is sustained to the shock, where the velocity then drops rapidly. At greater distances from the surface, the acceleration diminishes, and occurs increasingly farther downstream. At $y=2.03$ cm no acceleration is observed; only the shock-related drop is observed. The velocity decrease at the shock appears to extend over a streamwise distance of 1.5 cm. The bimodal LDV histograms clearly show that this gradual decline of mean speed is a manifestation of shock oscillations.

The normal component of the velocity (v) is illustrated in Fig. 20 in terms of streamwise distributions, at various distances from the wall. It is evident that the v -distributions for various y -values are similar, justifying the contention that extrapolation to the wall should be a reliable and accurate procedure for the determination of conditions at $y=0$. The distributions for $y=0.025$ cm are identical to those given in Fig. 11.

In the remainder of this section, comparisons between the two flows will be made using contour plots. The inevitable data scatter and the moderate density of the data points causes the plotting algorithm to generate physically meaningless detail in regions of small signal gradients. Omitting these details would be analogous to presenting smoothed data instead of the

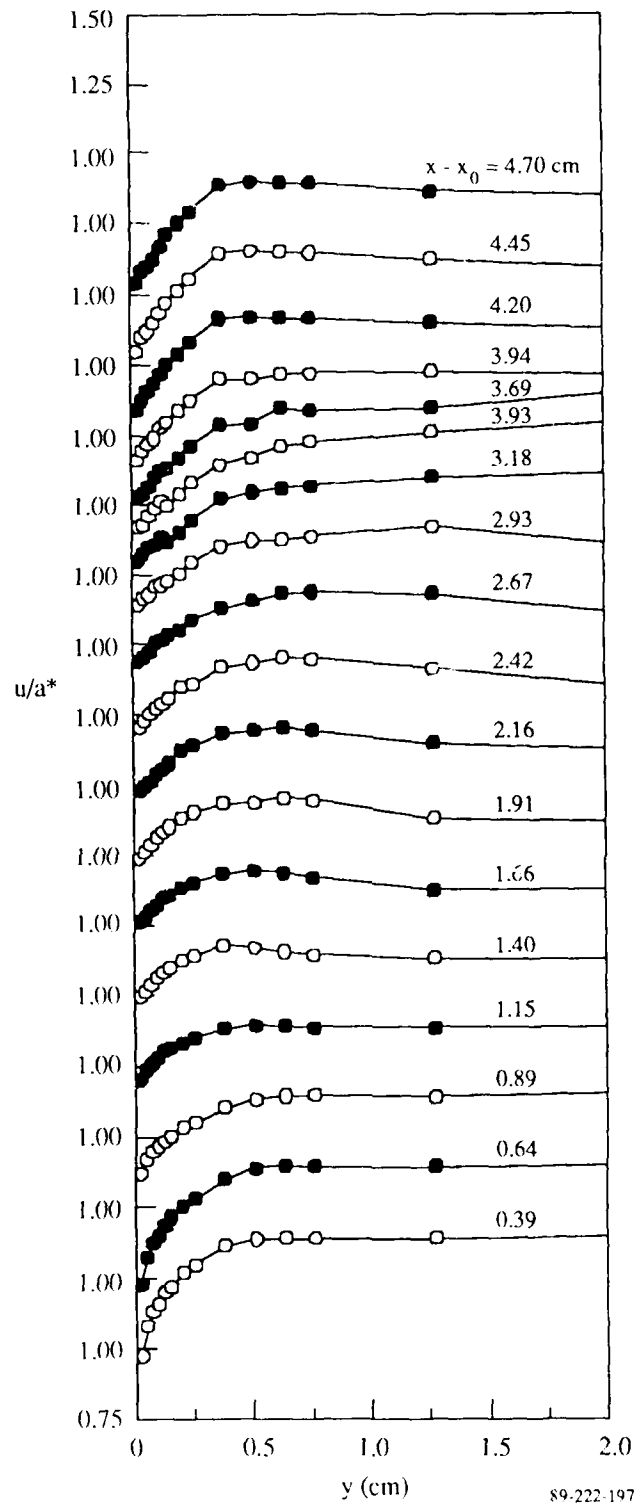


Figure 18. Profiles of u velocity component over the bleed zone, at densely spaced x -locations. Note high velocities at $y = 0$. The lowest tickmark labeled 1.00 on the vertical axis is assigned to $x - x_0 = 0.39$ cm. Curves and scales for greater values of $x - x_0$ are shifted successively upwards, by 0.25 each.

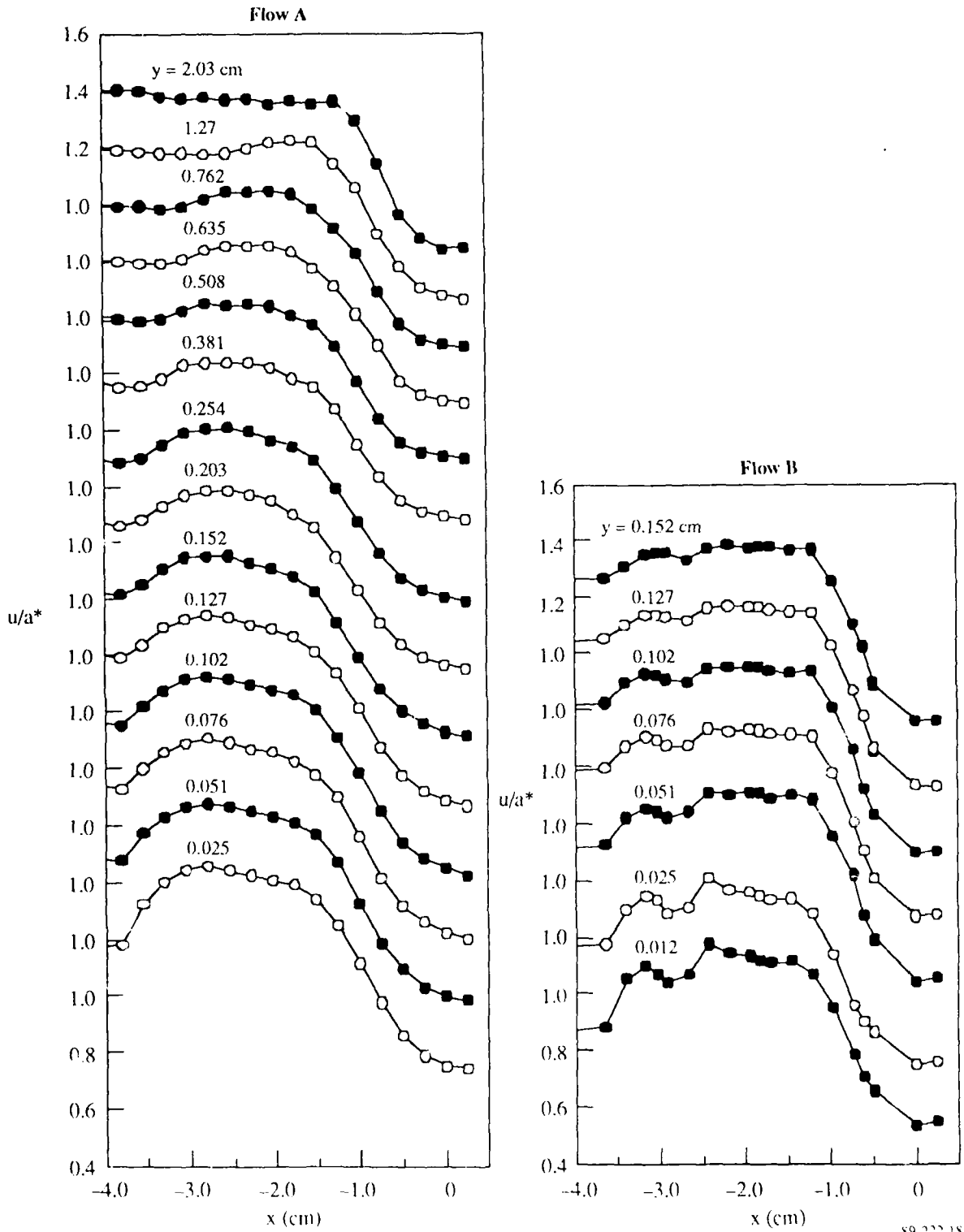


Figure 19. Streamwise distributions of u-velocity component at fixed distances from wall over bleed zone. The lowest tickmark labeled 1.0 on the vertical axis is assigned to $y = 0.022$ cm in both plots. Curves and scales for greater values of y are shifted successively upwards, by 0.2 each.

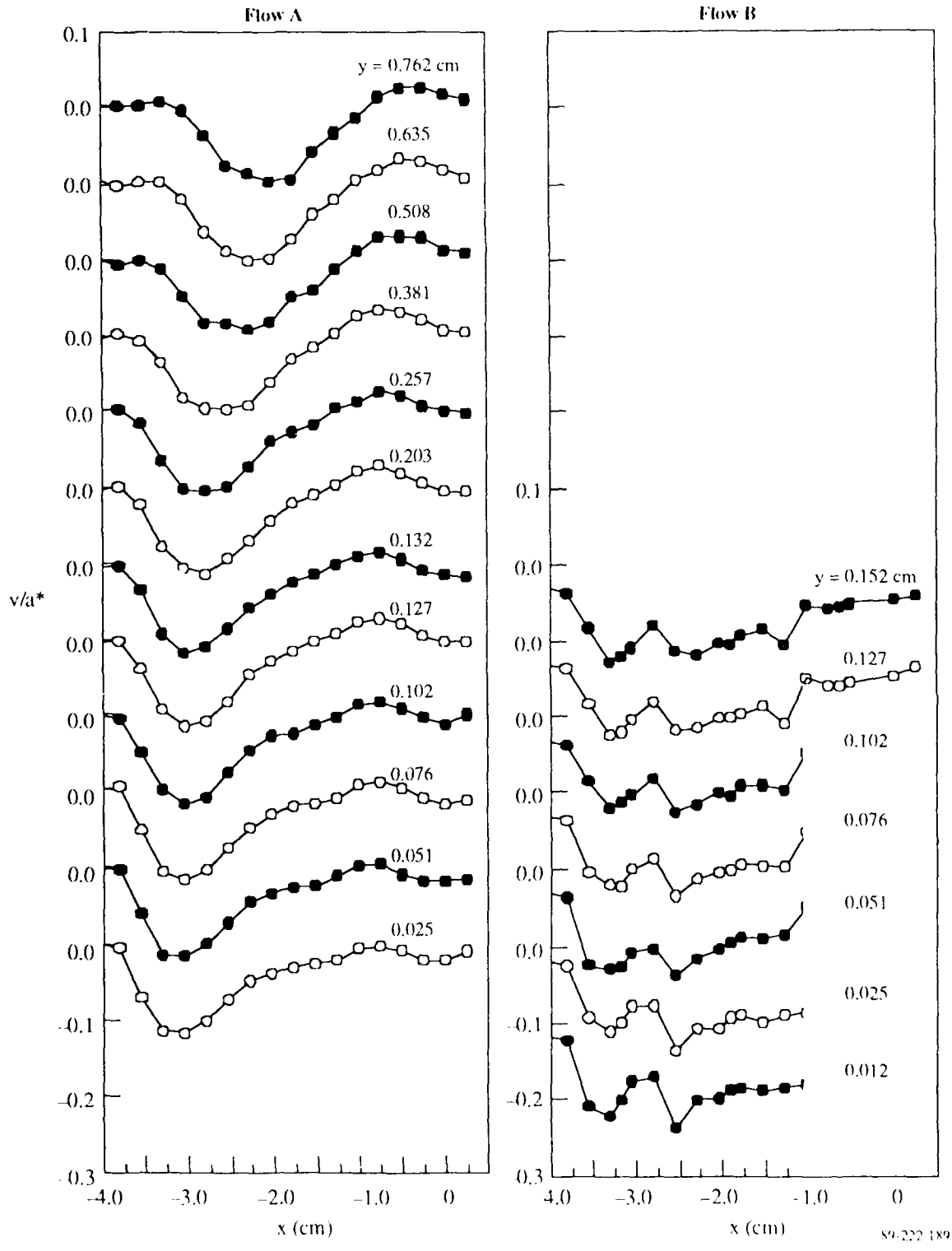


Figure 20. Streamwise distributions of v -velocity component at fixed distances from wall. The lowest zero on the vertical axis is assigned to the $y = 0.025$ cm curve for both flows. Curves and scales for other values of y are successively shifted vertically, by 0.1 each.

original data including the scatter, a procedure not appropriate for this report.

Figure 21 illustrates the u-component of the velocity. The plots show how the high-velocity regions approach the wall over the bleed region, i.e., how the wall velocities increase to values comparable to u_e . The evolution and disappearance of a low-speed region near the wall ($4 \text{ cm} < x-x_0 < 7.5 \text{ cm}$) is also evident: this is probably equivalent to the post-shock velocity minimum seen in Fig. 15. The shock does not possess the characteristic bifurcated structure that occurs in the absence of bleed: the shock is more or less normal to the wall at all values of y . The thick, smeared appearance is due to the streamwise oscillation of the shock. The expansion wave discussed in Fig. 10 is more or less observable: it creates a region of high velocity before the shock. The maximum normalized velocity is over 1.45 for flow A and over 1.40 for flow B. In terms of Mach number, these figures correspond to $M = 1.64$ and 1.56 , indicating a substantial acceleration due to the suction-induced deflection.

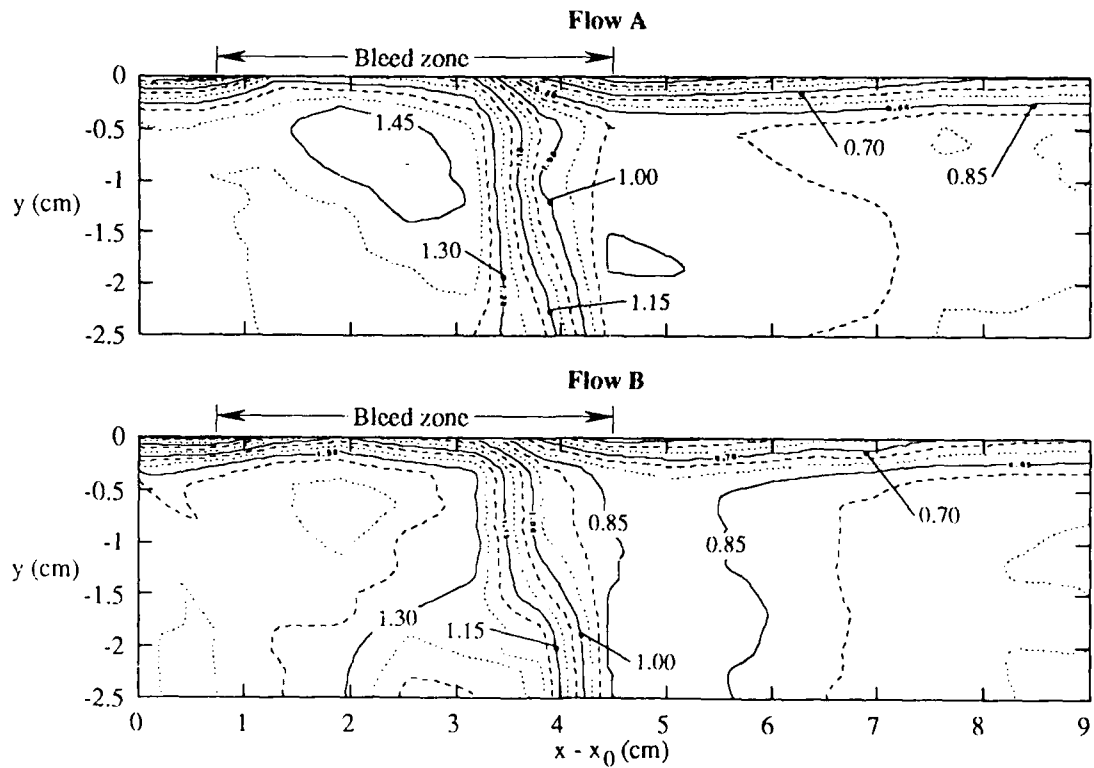
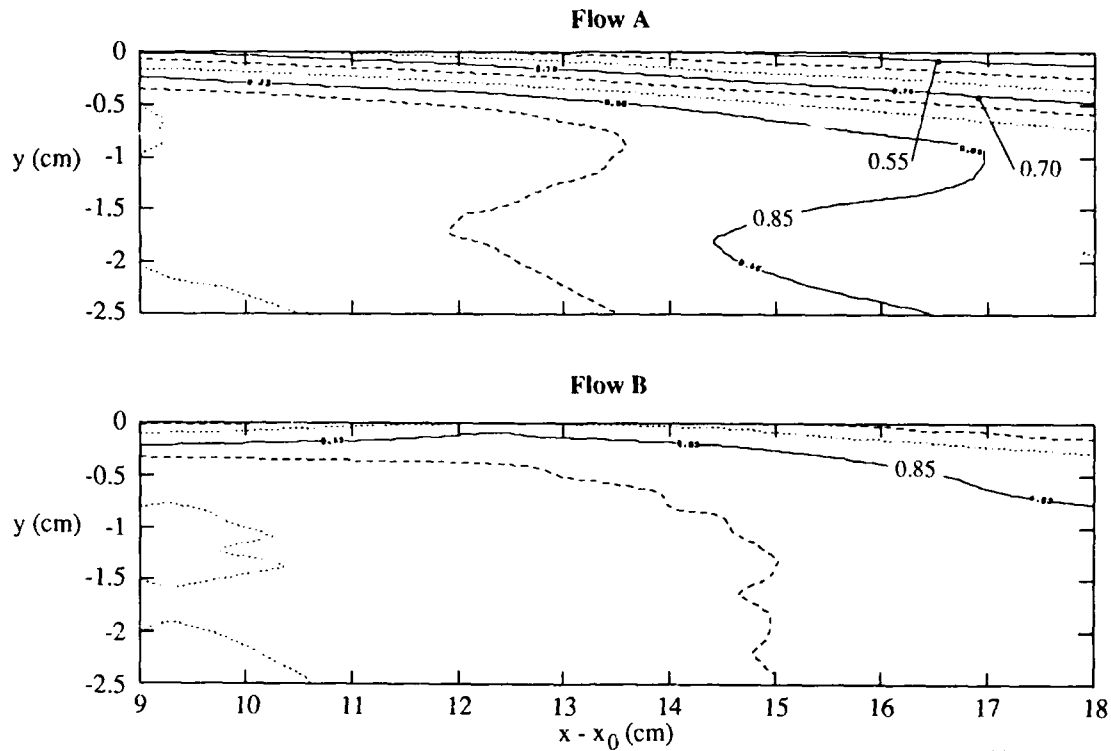


Figure 21a. Contours of $u/a^* = \text{constant}$ near the shock, for both flows.



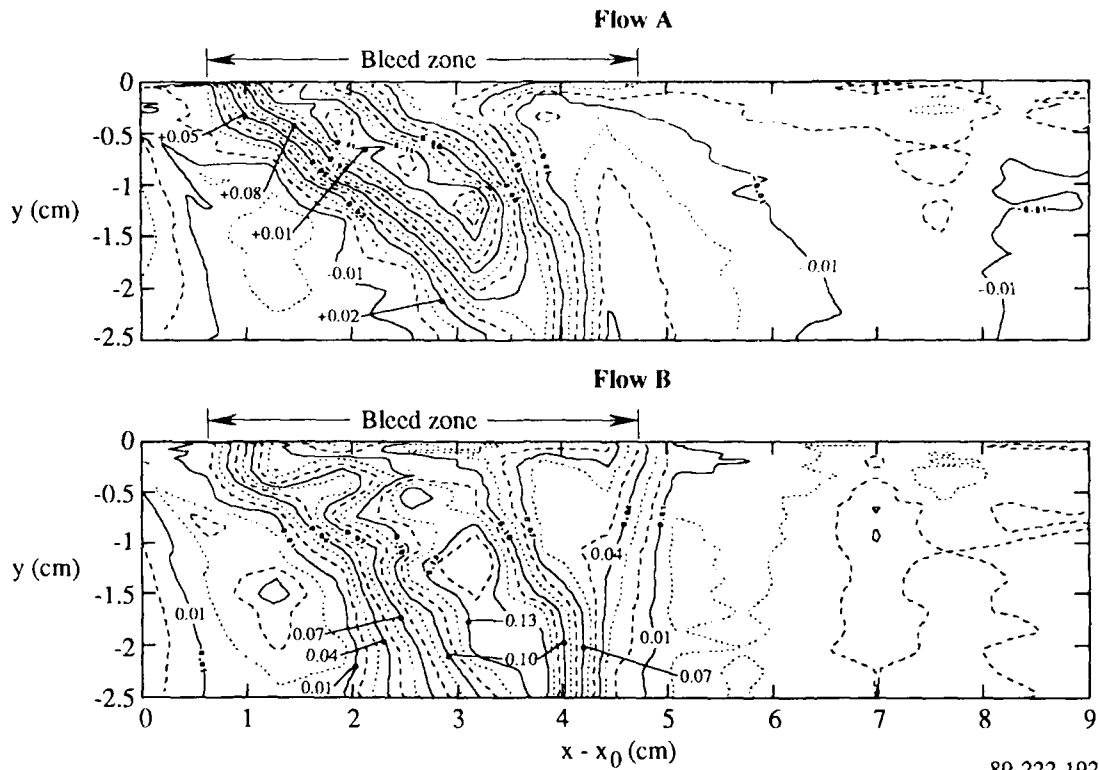
89-222-191

Figure 21b. Contours of $v/a^* = \text{constant}$ for $9 \text{ cm} < (x - x_0) < 18 \text{ cm}$, for both flows.

The velocity in the core flow reaches a minimum at or near $x - x_0 = 5 \text{ cm}$ and accelerates again to a local maximum at about 9 cm . The edge velocity displays a similar maximum (Fig. 15) at around $x - x_0 = 5 \text{ cm}$. Both of these maxima are symptoms of a subsonic re-acceleration caused by boundary-layer growth, the sidewall boundary layers being the most likely major contributors.

Figure 21b shows the downstream half of the flowfield, displaying a monotonic decrease of velocities and a thickening of the boundary layer in the recompressing, subsonic flow.

Figure 22 shows the v -components. The measurement of v is less accurate (it is obtained as the difference of two comparable frequencies detected by the LDV). The scatter is correspondingly greater and so is the proliferation of meaningless contour lines in areas where v is low. The plot does show the expansion waves, across which v changes from very low, inaccurate values, to significant magnitudes with a reasonable level of accuracy.



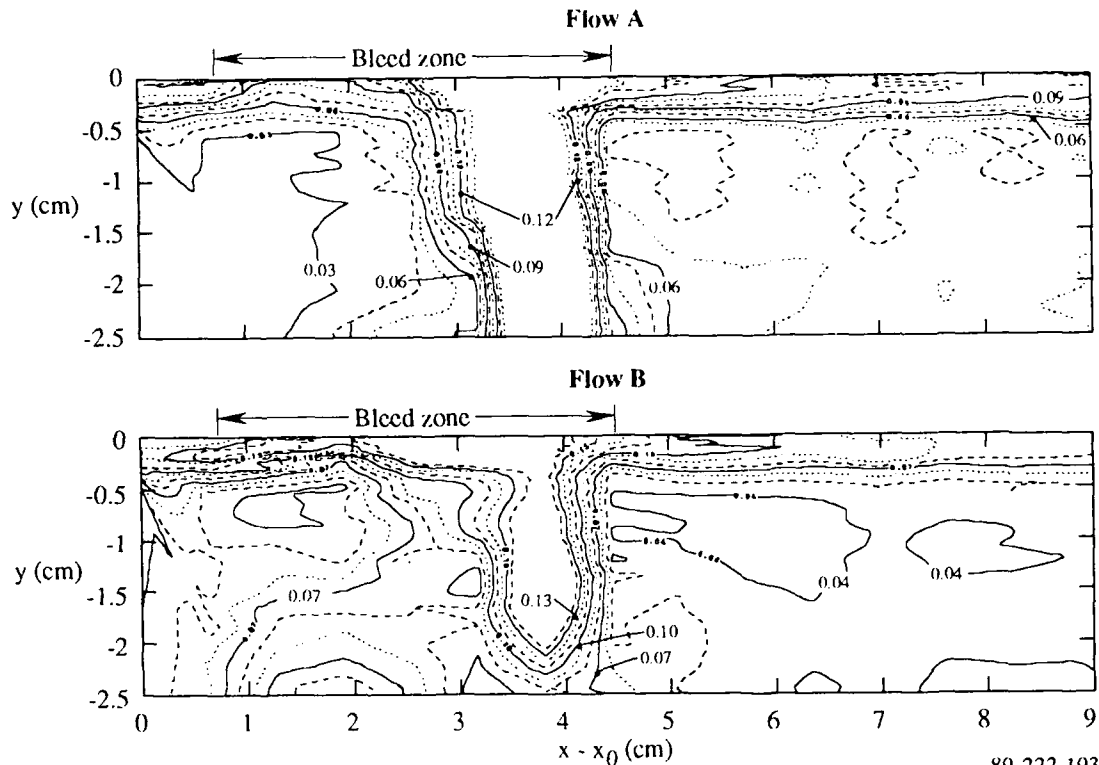
89-222-192

Figure 22. Contours of $v/a^* = \text{constant}$ near the shock, for both flows.

6.4 Turbulence Quantities

The rms value of the x-velocity component (\hat{u}) is illustrated in Fig. 23. High values were measured in the region swept out by the oscillating shock, because the system detects both the pre-shock and post-shock velocities that are very different. The contributions from two different speeds are clearly indicated by the bimodal histograms of the velocity data. The measured numbers are not necessarily meaningless, but their interpretation is beyond the scope of this contract. In this figure, contour lines with values greater than 0.15 were suppressed to allow the choice of scales that can reflect the turbulence intensity variations in the boundary layers, where the measurements are meaningful. The width of the blanked-out region indicates the spatial extent of the oscillations: the amplitudes are somewhat larger for flow A.

The intensities measured outside of the region occupied by the shock, e.g., in the boundary layers, represent valid information. Compared to uncontrolled interactions, in which the turbulence intensity may increase by



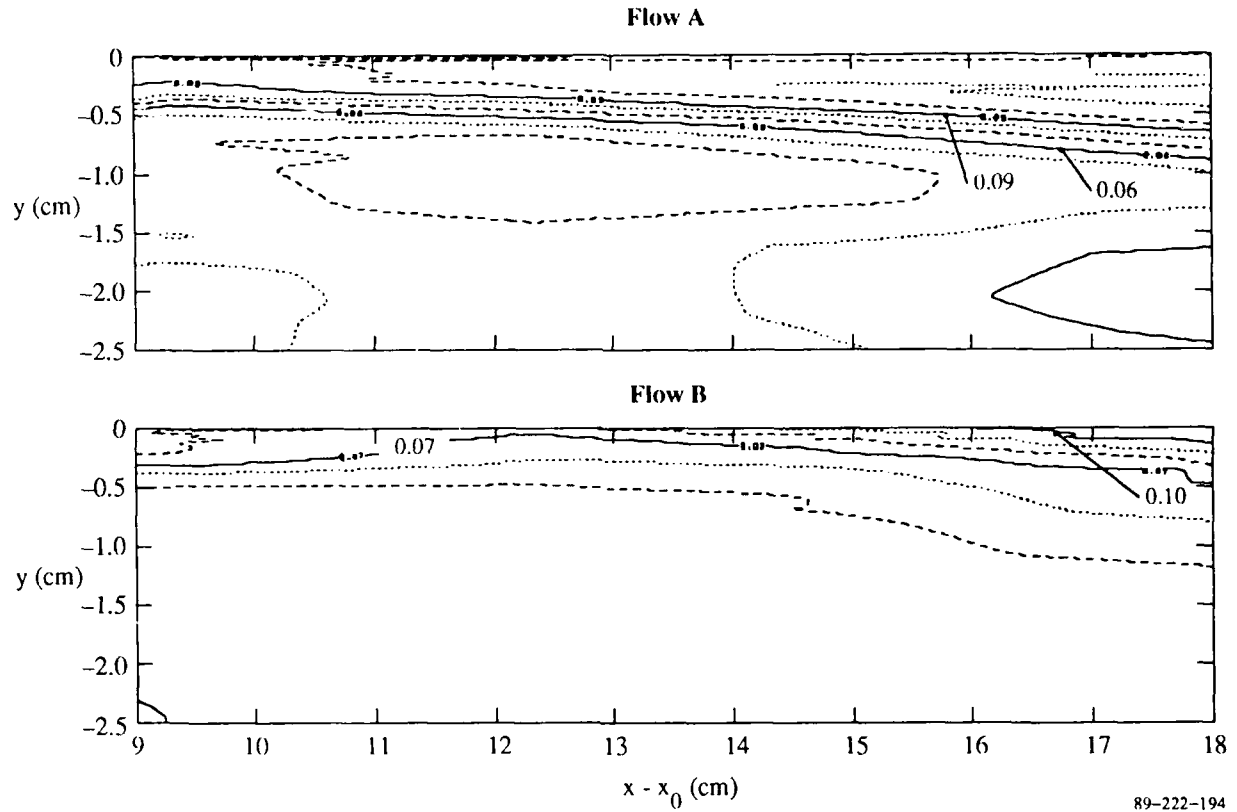
89-222-193

Figure 23a. Contours of $\hat{u}/a^* = \text{constant}$ near the shock, for both flows. Unrealistically high values occur in the region traversed by the shock during its oscillatory motion; values over 0.14 are omitted.

as much as a factor of ten, the turbulence intensities after the shock are very low. The fluctuations are of the same magnitude before and after the shock, i.e., the turbulence-enhancing influence of the interaction is completely neutralized by the mass removal.

The y component intensities (Fig. 24) also show some fluctuations related to the shock motion. However, the shock motion is primarily stream-wise and does not contribute much to the v-fluctuations. In the region occupied by the oscillating shock, the v-fluctuations are of the same order as the v-fluctuations in the boundary layer. In contrast, the u-fluctuations near the shock are 2-3 times larger than those within the boundary layers (Fig. 23).

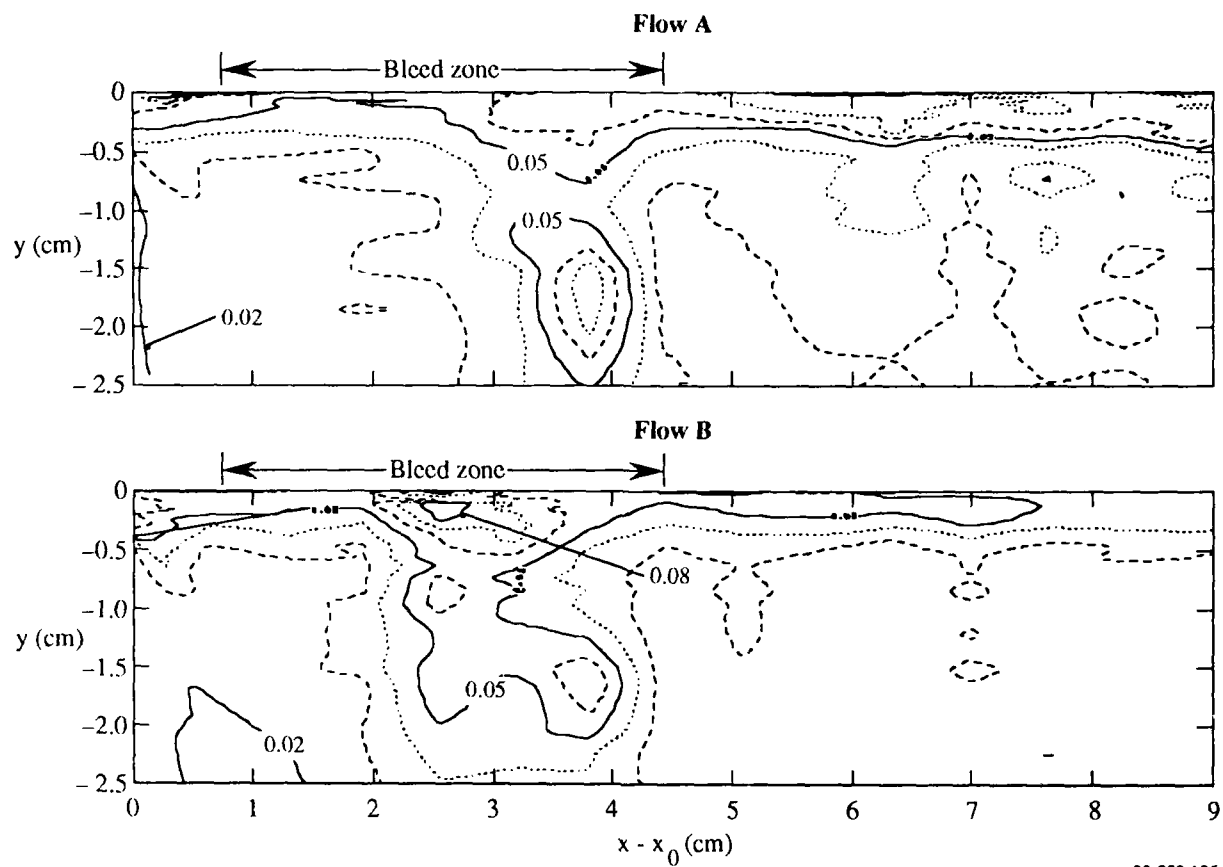
The Reynolds stress measurements are also strongly affected by the shock motion. Figure 25 shows high stresses in flow A, in the regions swept by the shock, while in flow B the highest stress regions occur where the bleed-induced expansion wave intersects the shock. In this region there are significant v-velocities which correlate well enough with the shock motion



89-222-194

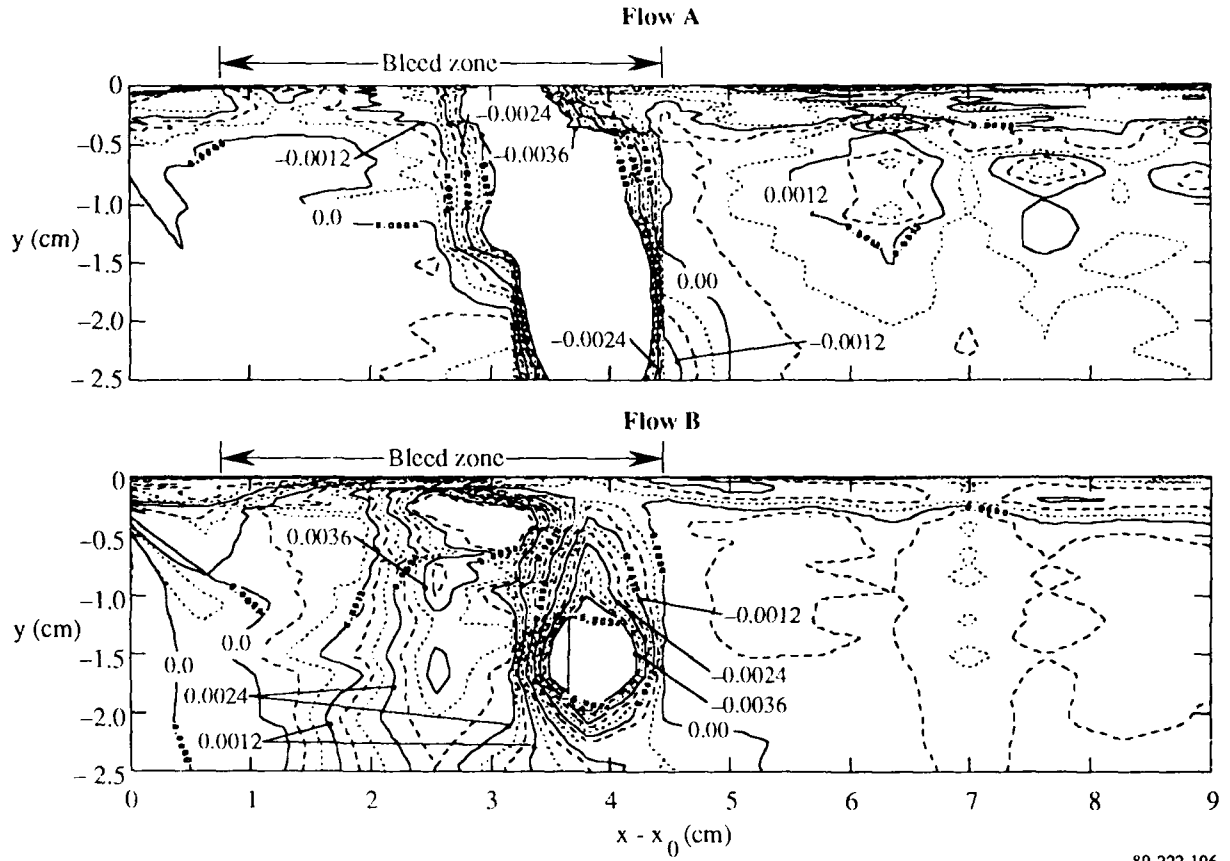
Figure 23b. Contours of \hat{u}/a^* for $9 \text{ cm} < (x - x_0) < 18 \text{ cm}$, for both flows.

to produce the apparent stresses. The stresses are notably higher in flow A. Regions where the stress measurements are believed to be degraded by the shock oscillation are blanked out, as they were in Fig. 23.



89-222-195

Figure 24. Contours of \hat{v}/a^* near the shock, for both flows.



89-222-196

Figure 25. Contours of $-\overline{u'v'}/a^*{}^2$ near the shock, for both flows. Unrealistically high values (over 0.004) in the region of oscillating shock are omitted.

7. SUMMARY AND CONCLUSIONS

Detailed measurements were made in two normal-shock/turbulent-boundary-layer interaction flowfields subject to mass removal. The approach Mach number was 1.49 and the Reynolds number based on approach momentum thickness was 14,000. The suction was applied upstream of a normal shock by using finely perforated plates of uniform open-area fraction over a distance corresponding to approximately 40 initial displacement thicknesses. The spatial average values of the normalized removed mass-flow were 0.025 and 0.08, for flows A and B, respectively. These values are representative of bleed rates employed in supersonic inlets. The perforated plate was located in the supersonic region just preceding the shock; other choices of location led to unacceptably large oscillations of the shock, and/or unacceptable distortion of the normal shock.

The imposition of suction initiated an expansion wave at the upstream edge of the bleed region. This wave created a region of higher velocity ahead of the shock (increasing the shock strength) and intersected the shock, thereby creating a weak shear layer in the subsonic flow.

In the absence of bleed, the interaction displayed small-amplitude shock oscillations (2-3 displacement thicknesses). The imposition of bleed caused the shock to oscillate randomly with an amplitude on the order of 10-15 boundary-layer displacement thicknesses.

In the regions swept out by the oscillating shock, the LDV measurements yielded false turbulence levels and Reynolds stresses (normal and shear) that resulted from correlating pre-shock and post-shock velocities. As a result, the Reynolds stresses cannot be interpreted in the conventional sense.

Mean and turbulent-fluctuation velocities were measured over the entire flowfield. The streamwise distribution of the local, normalized bleed rate [$\sigma(x)$] was nonuniform, especially in the case of the lower bleed rate (flow A).

The application of bleed changed the streamwise pressure distribution from a very gradual rise to a very abrupt one. There is evidence to suggest that the sharp pressure rise achieved by the application of suction to one of the channel walls caused flow separation on the two (unbled) side walls. (The sidewall boundary layers were attached when no mass removal was used.)

The boundary layer emerging from the controlled interaction has a somewhat distorted mean-velocity profile, but the magnitude of turbulent fluctuations is comparable to that of a normally developing boundary layer. In contrast, turbulence intensities may be amplified many times in uncontrolled interactions.

This investigation served the dual purpose of (a) exploring the physical features of two particular normal-shock/turbulent boundary layer interactions with mass removal and (b) generating a data base suitable for testing Navier-Stokes codes, in which the proper modeling of turbulence for SBLI's is still a largely unsettled issue. Both objectives were achieved.

The investigations documented a variety of flow features, some of which were anticipated, some of which were only conjectured to exist in the past and some of which were altogether unexpected. Mass removal-induced separation on adjacent solid walls, the existence of an expansion fan starting at the beginning of the bleed zone, and the distortion of the shock by the expansion fan were matters of speculation in the past. The low turbulence level in the post-shock boundary layer, the instability and unsteadiness of the shock in the interior of the bleed zone had not been anticipated. The results contradict the prevailing thought that suction generally exerts a stabilizing influence on SBLI's.

The figures of this report illustrate only a portion of the large data set that has been organized into computer files. Substantial amount of additional information is potentially extractable by further detailed analysis. The data are available to qualified investigators for validation of computer codes.

The work was too narrowly focused to allow the formulation of general guidelines concerning the design and performance of practical bleed systems, which may have many different geometric configurations and may operate under a great variety of conditions. The results clearly show, however, that the imposition of bleed has both favorable and adverse consequences on the flow within the channel. Inlet designers must be aware of the corresponding trade-offs and must evaluate them quantitatively to ensure an overall improvement.

This work could be continued in several profitable directions.

The presence of shock oscillations is the rule, rather than the exception in most transonic shock/boundary-layer interactions, external or

internal. The interpretation of LDV signals in the vicinity of an oscillating shock is extremely difficult and deserves a separate investigation. Diagnostic methods should be identified and developed to determine the time dependent velocity field near oscillating shocks.

The tendency of the shock to attach to the downstream edge of the bleed zone (i.e., shock instability at locations within the zone) needs to be explained theoretically, and the explanation needs to be verified experimentally. The study should include the cause of the increased level of unsteadiness observed with subsonic bleed.

Exploratory studies would be useful to find the practically important ranges for the characteristic parameters of bleed zones, such as streamwise extent, location, and suction flow rate. This information is considerable technological value by itself and it is also required for the selection of meaningful configurations for further detailed study.

8. REFERENCES

1. "Shock-Wave Boundary Layer Interactions," AGARD Report AG-280, Edited by Delery, J., and Marvin, J. G., Feb. 1986.
2. Salmon, J. T., Bogar, T. J. and Sajben, M., "Laser Doppler Measurements in Unsteady, Separated, Transonic Diffuser Flow," AIAA Journal 21(12), 1690-1697 (1983).
3. Schofield, W. H., "Interaction of a Turbulent Boundary Layer with a Normal Shock Wave Followed by an Adverse Pressure Gradient," Aeronautical Research Laboratories, Melbourne, Victoria, Rept. No. AR-002-950, Apr. 1983.
4. Wong, W. F., "The Application of Boundary Layer Suction to Suppress Strong Shock-Induced Separation in Supersonic Inlets," AIAA Paper 74-1063, Oct. 1974.
5. Delery, J., "Shock-Wave/Turbulent Boundary-Layer Interaction and its Control," Prog. Aerospace Sci. 22, 209-280 (1985).
6. Benhachmi, D., Greber, I. and Hingst, W., "Experimental and Numerical Investigation of an Oblique Shock Wave/Turbulent Boundary Layer Interaction with Continuous Suction," AIAA paper 89-0357, Jan. 1989.
7. Sajben, M., Morris, M. J., Bogar, T. J. and Kroutil, J. C., "Confined Normal-Shock/Turbulent-Boundary-Layer Interaction Followed by an Adverse Pressure Gradient," AIAA paper 89-0354, Jan 1989.

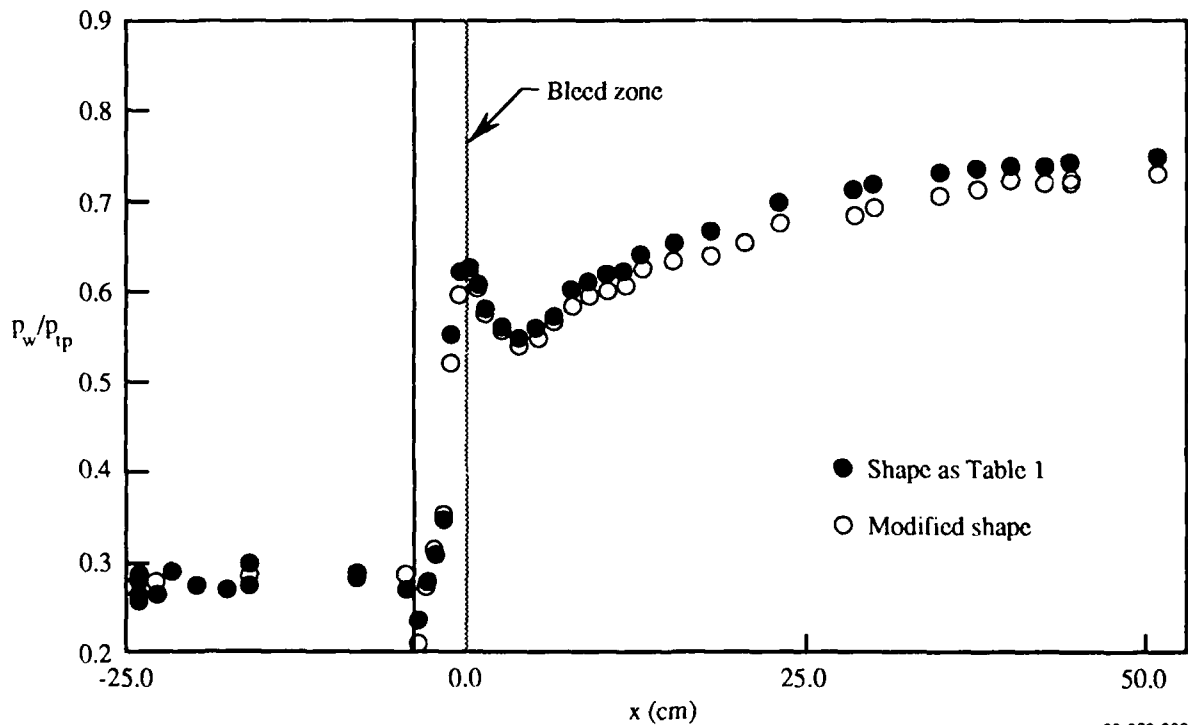
Appendix: Effect of Wall Contour Changes

The intent of installing the flexible wall was to control the pressure distribution in the subsonic region, and the wall is quite suitable for accomplishing this task over most of the diffuser.

The test showed that the imposition of mass removal drastically changes the pressure distribution in the immediate vicinity of the shock. Figure A-1 shows that the influence of the wall on this local variation is insufficient to effect a significant change.

The open symbols of Fig. A-1 represent the distribution obtained by increasing the channel height from 6.98 cm to 7.49 cm at the end. At the upstream end, the maximum deflections allowable by stress limitation were imposed.

Schlieren photographs showed that the large bottomwall curvature caused a separation of the bottom wall boundary-layer at the upstream end. This separation reduced, rather than increased the static pressure recovery. The



89-222-200

Figure A-1. Effect of wall contour change on topwall pressure distribution (Flow B).

modified pressure distribution (open symbols in Fig. A-1) lies below the original one. In the immediate neighborhood of the shock, the pressure distribution remained the same.

The conclusion was that the advantages of a parallel approach flow and a slot/shock-holder cannot be combined with those of a variable shape channel. Elimination of the bottom slot (which was not feasible within this program) would allow the utilization of the flexible wall for studying wall curvature effects on shock boundary-layer interactions, with only mildly divergent approach flows to the interaction.